Estimation of All-Sky Solar Irradiance Components over Rugged Terrain Using Satellite and Reanalysis Data
The Tibetan Plateau Experiment

Jia, Junru; Menenti, Massimo; Jia, Li; Chen, Qiting; Xu, Anlun

DOI
10.1109/TGRS.2024.3399702

Publication date
2024

Document Version
Final published version

Published in
IEEE Transactions on Geoscience and Remote Sensing

Citation (APA)
Jia, J., Menenti, M., Jia, L., Chen, Q., & Xu, A. (2024). Estimation of All-Sky Solar Irradiance Components over Rugged Terrain Using Satellite and Reanalysis Data: The Tibetan Plateau Experiment. *IEEE Transactions on Geoscience and Remote Sensing*, *62*, 1-23. Article 4104423. https://doi.org/10.1109/TGRS.2024.3399702

Estimation of All-Sky Solar Irradiance Components Over Rugged Terrain Using Satellite and Reanalysis Data: The Tibetan Plateau Experiment

Junru Jia, Massimo Menenti, Li Jia, *Member, IEEE*, Qiting Chen, and Anlun Xu

***Abstract*— Accurate knowledge of the at-surface solar irradiance (SSI) is essential for retrieving surface and atmospheric properties using satellite measurements of backscattered and reflected radiance. The latter is affected by surface–atmosphere interactions, including the effects of terrain. The SSI is affected by the same processes. This study proposes a method to estimate the components of instantaneous SSI: direct, isotropic and circumsolar diffuse, and terrain irradiance, which is expected to improve the simultaneous retrieval of aerosol optical depth (AOD) and surface reflectance. The method takes into account the coupled effects of topography and atmosphere by combining parameterization and the lookup table (LUT) approaches. The method was applied to rugged terrain over the Tibetan Plateau using Moderate Resolution Imaging Spectrometer (MODIS) atmosphere and surface data, the fifth generation European Centre for Medium-Range Weather Forecasts reanalysis (ERA5) data, Cloud-Aerosol Lidar With Orthogonal Polarization (CALIOP) aerosol data, and a digital elevation model (DEM). The results showed that the SSI estimates were in satisfactory agreement with ground observations at four stations over the Tibetan Plateau (TP) in 2018 with R^2 values of 0.61, 0.44, 0.41, and 0.49, respectively, and root mean square error (RMSE) of 205.7, 176.9, 186.0, and 201.2 W/m^2, respectively. Estimations of the diffuse irradiance were evaluated separately against the only available in situ observations at the Dali Station, and the results were better than our SSI estimates with R^2, RMSE, and relative bias (BIAS) being 0.71, 94.98 W/m^2, and 31%, respectively. The isotropic and circumsolar diffuse irradiances accounted for 37.57% and 7.68% of the total annual SSI, respectively, while diffuse irradiance accounted for 46.48% of the total annual SSI. Under clear skies, every 0.1 increase in AOD caused about a 35-W/m^2 increase in diffuse irradiance and a decrease of about 25 W/m^2 of SSI.**

***Index Terms*— Circumsolar diffuse irradiance, isotropic diffuse irradiance, rugged terrain, sky diffuse irradiance, solar irradiance, terrain irradiance.**

I. Introduction

THE surface solar irradiance (SSI) in the spectral domain of 300–4000 nm drives the energy budget of the Earth's surface and the general circulation of the atmosphere through radiative heating. Accurate knowledge of SSI is also critical for improving the accuracy of the surface and atmospheric properties retrieved from satellite measurements, such as surface albedo and aerosol quantity and size distribution.

The Tibetan Plateau is the highest and largest plateau in the world with a mean elevation of approximately 4500 meters above sea level (m.a.s.l.) and is known as the Water Tower of Asia because it is the third largest reservoir of water ice in the world. The energy balance and SSI of the Tibetan Plateau, a high-elevation heat and water source, significantly influence both regional and global climates.

In mountainous areas, the SSI received by a facet of an inclined surface consists of four components: the direct, isotropic diffuse, circumsolar diffuse, and surrounding terrain irradiances [1]. Currently, the methods to estimate the SSI can be classified into five groups: 1) radiative transfer models; 2) physics-based relationships; 3) parameterization methods; 4) lookup table (LUT) method; and 5) other methods. The radiative transfer models simulate the detailed processes and interactions of the transfer of solar radiation in the atmosphere [2], [3], [4]. If detailed vertical distributions of the atmospheric constituents are known, the SSI can be accurately estimated using a radiative transfer model. However, the application of radiative transfer models at regional scales is usually limited due to the large computing resources and the requirement of a substantial input of variables/parameters, which is usually difficult to obtain at the regional scale. Relationships between satellite observations and ground measurements may be established to estimate the SSI using simplified regression formulas. Such regression methods are simple and easily implemented [5], [6], but the relationship determined for a specific region is usually difficult to apply in

Manuscript received 9 August 2023; revised 15 December 2023 and 28 February 2024; accepted 27 March 2024. Date of publication 17 May 2024; date of current version 23 May 2024. This work was supported in part by the Second Tibetan Plateau Scientific Expedition and Research Program (STEP) under Grant 2019QZKK0103 and in part by the National Natural Science Foundation of China Project under Grant 91737205. The work of Massimo Menenti was supported in part by the Chinese Academy of Sciences President's International Fellowship Initiative under Grant 2020VTA0001 and in part by the Ministry of Science and Technology (MOST) High Level Foreign Expert Program under Grant GL20200161002. *(Corresponding author: Li Jia.)*

Junru Jia is with the Key Laboratory of Remote Sensing and Digital Earth, Aerospace Information Research Institute, Chinese Academy of Sciences, Beijing 100101, China, and also with the University of Chinese Academy of Sciences, Beijing 100049, China (e-mail: jiajr@radi.ac.cn).

Massimo Menenti is with the Key Laboratory of Remote Sensing and Digital Earth, Aerospace Information Research Institute, Chinese Academy of Sciences, Beijing 100101, China, and also with the Faculty of Civil Engineering and Earth Sciences, Delft University of Technology, 2628 CN Delft, The Netherlands (e-mail: m.menenti@tudelft.nl).

Li Jia and Qiting Chen are with the Key Laboratory of Remote Sensing and Digital Earth, Aerospace Information Research Institute, Chinese Academy of Sciences, Beijing 100101, China (e-mail: jiali@aircas.ac.cn; chenqt@aircas.ac.cn).

Anlun Xu is with the Dali National Climate Observatory, Dali 671003, China (e-mail: xualun@126.com).

Digital Object Identifier 10.1109/TGRS.2024.3399702

other regions [7]. This may apply particularly to relationships established by applying AI algorithms, while physics-based relationships, such as [5], are more generally applicable [8], [9], [10], [11], [12]. Parameterization methods are based on physical processes, but the estimate of the SSI as a function of water vapor, aerosol optical depth (AOD), and thickness of the ozone layer is simplified [13], [14], [15]. Most of the existing parameterization methods have been established for clear-sky conditions, and their results are in good agreement with the ground observations [14], [16], [17]. Parameterizations for cloudy-sky have been extensively studied. Despite the complex variations in the microphysical and optical properties of clouds, modern techniques and methodologies, such as the ones applied to generate the all-sky data provided by the Satellite Application Facility on Climate Monitoring (CM-SAF), have enabled the accurate simulation of the attenuation effects of clouds on radiative flux. LUTs are generated using atmospheric radiative transfer models applied to a large number of cases. The model results are resampled to construct an applicable LUT to retrieve SSI. Liang et al. [18] proposed the LUT approach to estimate the instantaneous incident photosynthetically active radiation (PAR) from Moderate Resolution Imaging Spectrometer (MODIS) data. Zhang et al. [19] used precalculated offline LUTs with different atmospheric input data for clear and cloudy skies. These methods based on LUTs avoid using complex input parameters. There are also other estimation methods, such as the method of combining empirical relationships with physical methods [8], [9], optimization methods [20], and machine learning methods [21], [22], [23].

A flat terrain is assumed when retrieving the atmospheric and surface properties in most algorithms, leading to significant errors and uncertainties in the retrieved SSI over rugged terrain. In recent years, some researchers have achieved good SSI results by considering terrain effects [24], [25], [26]. Wang et al. [26] developed a shortwave radiation model (SWTRM) by applying an artificial neural network to quantify the direct solar radiation and taking into account the effects of the shading, surrounding terrain, and sky shielding in mountainous regions. Although the calculated results are quite consistent with the ground measurements, the model has not been used frequently because it needs to be retrained if the radiometric input data are changed [26]. In addition, the impact of the terrain characteristics on the SSI changes under different atmospheric conditions, and this aspect has not received sufficient attention. One alternative method that has been developed to estimate SSI over complex terrain is HelioMont [27]. This method uses a combination of ground-based and satellite observations, along with topographic and atmospheric data, to estimate daily and monthly average SSI over rugged terrain.

Under clear-sky conditions, a substantial fraction of the irradiance received by the surface that is unobstructed by the topography is direct solar radiation. In contrast, under cloudy or hazy conditions, scattering increases, and the fraction of incoming diffuse radiation increases, resulting in a more uniform irradiance on the surface [28].

Solar radiation is absorbed and scattered by gases and aerosols in the atmosphere. Aerosols are one of the most important atmospheric factors affecting solar radiation through absorption and scattering. Black carbon and other light-absorbing aerosols can be deposited on the surface, thus increasing the total absorption of solar radiation, which can accelerate the melting of ice and snow, thus affecting the surface energy and mass budgets of the Tibetan Plateau. Ramanathan and Carmichael [29] found that the radiative forcing by black carbon, one of the most potent light-absorbing aerosols, is likely to be one of the largest contributors to climate warming after carbon dioxide. Wild et al. [30] found that a 10% increase in AOD can lead to a 2.7% decrease in global mean surface solar radiation. Wang et al. [12] found that the impact of aerosols on the radiation budget of the Tibetan Plateau is significant due to the high altitude and low atmospheric pressure of the region, which makes it highly sensitive to changes in solar radiation. The Tibetan Plateau is highly sensitive to changes in radiation due to its high elevation and relatively small atmospheric optical depth. Even a small increase in aerosol concentration can have significant impacts on surface energy and mass budgets. Aerosols can also affect cloud formation and their lifetime, further affecting the radiation budget of the earth–atmosphere system.

Gaps in satellite retrievals of atmospheric properties are frequent in the Tibetan Plateau partially due to extremely high altitude, heterogeneity, and the difficulty of estimating correctly the background surface leaving radiance. The same uncertainties result in the difficulty of estimating the downwelling shortwave radiation correctly [31], [32]. In several previous studies, the aerosol load was taken into account by using the average of observations of AOD on the Tibetan Plateau due to the lack of instantaneous observations for estimating SSI [33], [34]. Several researchers have reported that the natural and anthropogenic aerosol concentrations increase at altitudes of 6–8 km above sea level (a.s.l.) over the Tibetan Plateau [35], [36], [37]. According to the findings of the study [35], there is a noticeable distinction in dust occurrence between the northern and southern Tibetan Plateau, which becomes clear at an altitude of 6-8 km a.s.l., particularly in spring and summer. Further comprehensive research and discussions are necessary to understand the mechanisms behind the transport of dust from the atmospheric boundary layer into the upper troposphere and lower stratosphere during spring. The dust layer can extend up to the upper troposphere and lower stratosphere in spring, reaching altitudes of approximately 11–12 km, whereas, in other seasons, it is observed at much lower elevations [35]. This pattern of higher dust occurrence in the north and lower dust occurrence in the south is observed, with the divide located around 33°N–35°N in the middle of the Plateau, and it extends from the surface up to an altitude of 6–8 km [35]. A significant quantity of anthropogenic aerosol is also transported from Eastern China to the east of the TP by easterly winds [37]. The long-distance transport of aerosols usually occurs in the upper troposphere. The Tibetan Plateau is located in the vicinity of several important natural and anthropogenic aerosol sources, and these aerosols can be transported over the Tibetan Plateau [37], [38], [39], [40]. However, due to the unique topographic characteristics and altitude of the Tibetan Plateau, the widely used atmospheric profiles in atmospheric correction methods deviate from the actual situation on the Tibetan Plateau [41]. The combination of complex topography and the heterogeneity of the land surface (i.e., vegetation, bare soils, lakes, Gobi, sandy desert, snow, and ice interspersed with meltwater) make it even more important to account for the terrain effects. On the Tibetan Plateau, the retrieval of both the surface and atmospheric variables from satellite radiometric data is affected by the large uncertainty caused by these complex radiation–target interactions.

The main goal of this study was to develop a method for calculating SSI and its four components (i.e., direct, isotropic diffuse, circumsolar diffuse, and surrounding terrain irradiances) on the Tibetan Plateau with 1-km resolution. This study is a contribution to a broader study to retrieve surface spectral reflectance, albedo, and AOD simultaneously based on the correct angular distribution of the direct and diffuse components of instantaneous downwelling radiance. The design of our method is a consequence of the need for instantaneous information on SSI and its components at the MODIS overpass time. We aimed at taking into account not only the atmospheric effects but also the impact of the surrounding terrain on irradiance at the observed target. First, we used a combination of parameterizations and an LUT scheme to estimate atmospheric absorption and diffuse radiation to obtain SSI assuming a flat surface under clear- and cloudy-sky conditions on the Tibetan Plateau. The parameterization scheme requires more input data and has a relatively high computational efficiency, while the LUT scheme requires less input data but has a lower computational efficiency. Second, a radiative transfer model combined with the parameterizations and the LUT scheme was used to accurately estimate the SSI and its four components, taking into account the influence of the topography on a tilted surface. The results were validated using instantaneous daily SSI observations obtained at four experimental stations on the Tibetan Plateau.

II. Study Area and Data Description

A. Study Area and In Situ Radiation Observations

The Tibetan Plateau is bordered to the south by the inner Himalayan range, to the north by the Arkin Qilian Mountains, to the west by the Karakorum Mountains, and to the east by the Hengduan Mountains. The Tibetan Plateau is surrounded by massive mountain ranges in the high-mountain region of Asia (see Fig. 1). It accounts for 25% of China's land area, with a total area of approximately 2.05 million km^2 and an average altitude of more than 4500 m.a.s.l. It is the largest plateau in China and the highest plateau in the world. The ground measurements were obtained from radiation balance stations located on the Tibetan Plateau (see Table I and Fig. 1), namely, the Dali Station, the Linzhi Station, the Muztagh Ata Station for Westerly Environment Observation and Research Station (MAWORS), and the Qomolangma Atmospheric and Environmental Observation and Research Station (QOMS). Each station offers unique insights into different atmospheric and environmental aspects, enhancing the overall representativeness of the study. These stations, with MAWORS in the westerly zone and QOMS, Linzhi, and Dali in the monsoon zone, are geographically and climatically positioned to represent different terrain conditions, ecosystem types, and climate zones on the Tibetan Plateau. QOMS, Linzhi, and Dali Stations are located in the monsoon climate influence zone. Detailed information about the locations and the instruments for Linzhi Station, MWWORS, and QOMS can be found in [42] and [43]. The QOMS Station, a key component of the "Third Pole Environment" (TPE) program is situated at an elevation of 4298 m.a.s.l., 30 km from the northern boundary of Mount Everest. It is located in a semiarid plateau monsoon climate, characterized by an alpine Gobi desert with relatively flat open terrain, primarily composed of bare ground and sparse, short vegetation. It plays a vital role in the TPE program by contributing valuable data on desert meadow ecosystems. The MAWORS Station is positioned at 3668 m.a.s.l. in the zone influenced by the westerly climate near Muztagh Ata Mountain and Karakul Lake. It provides essential data on the impact of westerly driven weather, which leads to a dry and cold climate [44]. The Linzhi Station, located at 2991 m.a.s.l., is situated in a valley with dense vegetation of temperate coniferous trees and alpine meadows, and it offers critical insights into soil moisture and hydrological processes in well-developed shallow soils [45]. It is also influenced by the warm and moist air currents from the Bay of Bengal, resulting in frequent cloudiness and rainfall. The land cover is a plateau meadow surrounded by forest land, and the vegetation has good growing conditions. The Dali Station, 1999 m.a.s.l., is located in the valley between the Cangshan Mountains in the west and the Erhai Lake in the east, which is in Henduan Mountains along the key water vapor transport channel on the southeast edge of the Tibetan Plateau. It is in the windward zone of the Southwest Monsoon of the Bay of Bengal, belonging to the subtropical highland monsoon climate type.

The land cover at the four sites changes a lot from desert and Alpine steppe to farmland. The terrain conditions and ecosystems are rather different. The four radiation balance components (downward and upward shortwave and longwave radiations) were measured on a mast at 1.5 m above the ground, where also the diffused irradiance was measured. Our evaluation is done using daily instantaneous estimates for a period of one year at the MODIS Aqua overpass time, i.e., sampling a wide range of atmospheric conditions. The stations that we used are located at key locations in diverse ecological and climatic zones, enhancing the usefulness of the data to evaluate our method.

B. Satellite Data

1) MODIS Data: The MODIS sensors onboard the Terra and Aqua satellites acquire images in 36 spectral bands between 0.62 and 14.385 μm with a wide ground swath of ~2330 km. The spatial resolutions in the different spectral bands are 250 m, 500 m, and 1 km. The MODIS level 1B data are radiometrically calibrated, and the level 2 data are in an ungridded orbital swath format, where each swath is divided into small segments or granules (one file with a 5-minute duration). MODIS Aqua data were used in this study. Aqua and the Cloud-Aerosol LiDAR and Infrared Pathfinder

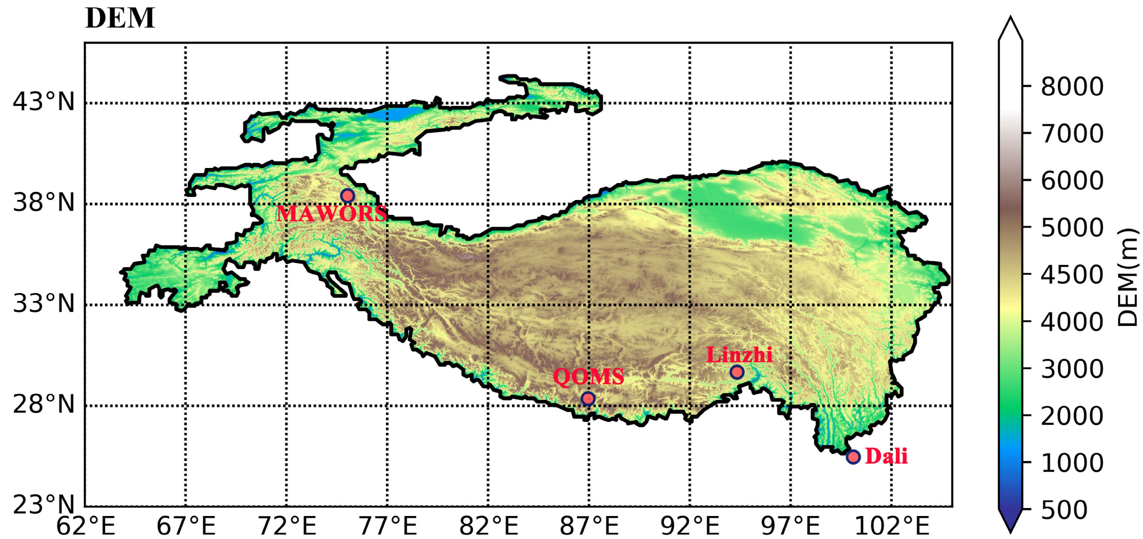

Fig. 1. DEM map of the third pole showing the study area and locations of the ground stations (red dots).

TABLE I
GEOGRAPHIC CHARACTERISTICS OF THE FOUR SITES WITH RADIATION MEASUREMENTS ON THE TIBETAN PLATEAU

	Latitude	Longitude	Elevation (m.a.s.l)	Slope (30m)	Aspect (30m)	Land cover	Soil type	Slope (1km)	Aspect (1km)
MAWORS	38.42°N	75.03°E	3668m	5°	119°	Alpine desert	Sand and gravel	19°	106°
Linzhi	29.67°N	94.33°E	2991.8m	2°	11°	Alpine steppe	Sand and gravel	12°	155°
QOMS	28.36°N	86.95°E	4298m	7°	45°	Alpine desert	Sand and gravel	8°	172°
Dali	25.72°N	100.19°E	1990m	3°	309°	Farmland	Paddy soil	3°	109°

Satellite Observation (CALIPSO) are members of the "A-Train" satellite constellation and observe the same location at nearly the same time [46]. In this study, the MODIS atmospheric products, including MYD04 L2 (aerosol optical thickness) and MYD05 L2 (total precipitable water vapor), were used as input data (see Table II). Eight variables, AOD, precipitable water content, ozone optical depth, surface pressure, cloud top pressure, cloud fraction (cf), and cloud optical depth, i.e., the MODIS atmospheric data products, were used to estimate the atmospheric transmittance. The geolocation of the observations was obtained from MYD03. MYD09_L2 is a surface reflectance data product from MODIS Aqua, which was used to estimate the terrain irradiance by integrating the spectral reflectance from 400 to 2155 nm.

TABLE II
MODIS LEVEL-2 DATA PRODUCTS USED IN THIS STUDY

Product short name	Product name	Spatial resolution	Temporal resolution	Data type
MYD03	Geolocation dataset	1 km	5 minutes	Longitude/latitude
MYD04 L2	Aerosol optical thickness	10 km	5 minutes	Corrected optical depth land
MYD05 L2	Total precipitable water vapor	1 km	5 minutes	Water vapor Near Infrared
MYD06 L2	Cloud	1 km or 5k m	5 minutes	Surface pressure Cloud top pressure Cloud fraction day Cloud optical thickness
MYD07 L2	Atmosphere profile	5 km	5 minutes	Total ozone
MYD09 L2	Surface reflectance	1 km	5 minutes	Surface reflectance

2) CALIOP Data: The Cloud-Aerosol LiDAR With Orthogonal Polarization (CALIOP), onboard the CALIPSO, has been acquiring global aerosol and cloud profile data since June 2006 [47]. It acquires LiDAR backscatter profiles at 532 and 1064 nm, including parallel and perpendicular polarized returns at 532 nm. The profiles are sampled at a vertical resolution of 30 m below an altitude of 8.2 km and at a 60-m resolution between 8.2 and 20.2 km [48]. The CALIOP

Level 2 data contain curtains of retrieved profile data along the CALIPSO orbit [48]. The CALIOP Level 2 5-km aerosol products contain height-resolved geophysical variables, such as aerosol backscatter, extinction, depolarization, and the results of the aerosol type classification. Uncertainty estimates are included for each retrieved variable, along with data quality flags. CALIPSO is in a Sun-synchronous orbit with an equator crossing time of ~2 P.M. and a 16-day orbit repeat cycle. Aqua and CALIPSO are in a constellation flight, each moving along a circular orbit constrained inside their respective control boxes. Due to this arrangement, CALIPSO is never more than 118 s behind Aqua. We used the Extinction_Coefficient_532 dataset and the CALIOP Level 2 5-km aerosol profile to obtain the surface aerosol extinction, along with the fifth generation European Centre for Medium-Range Weather Forecasts reanalysis (ERA5) data, as input to the moderate resolution atmospheric transmission (MODTRAN) model. When the CALIPSO Level 2 value was not available, we used the monthly CALIPSO L3 Extinction_Coefficient_532_Mean value.

3) Topographic Data: The slope and aspect of the terrain were retrieved at a 30-m resolution from the digital elevation model (DEM) generated using the data acquired by the Advanced Spaceborne Thermal Emission and Reflection Radiometer (ASTER), i.e., the global DEM version 2 (GDEM2). The ASTER-GDEM2 is one of the most widely used high-resolution digital topographic datasets to date. The 30-m resolution ASTER-GDEM2 data were averaged to estimate the mean elevation of each 1 × 1 km grid, i.e., the same spatial resolution as the MODIS surface reflectance data. The slope and aspect for each 1 × 1 km were calculated by taking the (dz/dx) and (dz/dy) components of the elevation difference in a 3 × 3 window centered on the target pixel and then calculating the slope as $\tan^{-1}((((dz/dx))^2 + ((dz/dy))^2))^{1/2}$ and the aspect as $\tan^{-1}(((dz/dx))/((dz/dx))) + \pi$. Even though some geolocation errors and elevation aberrations have been identified at the global scale, this dataset remains the best alternative regarding accessible high-quality elevation data for the selected study area [49]. Fig. 2 shows the 1-km degraded resolution DEM, slope, aspect, sky-view factor (SVF), and terrain view factor (TVF) from the ASTER-GDEM2 for the Aqua MODIS overpass at 07:15 Coordinated Universal Time (UTM) on January 2, 2018. The definitions and the equations to compute SVF and TVF can be found in Section III-B.

C. ERA5 Reanalysis Data

The ERA5 is the fifth-generation reanalysis dataset generated by the European Center for Medium-Range Weather Forecasts (ECMWF) for global climate and weather studies, and it covers the past seven decades. The ERA5 provides hourly estimates of a large number of atmospheric, land, and oceanic climate variables. The data cover the Earth using a 30 × 30 km grid, and 137 levels from the surface to an altitude of 80 km are applied to describe the vertical structure of the atmosphere. The ERA5 hourly pressure level data have been regridded to a 0.25° regular latitude–longitude grid. The ERA5 atmospheric variables used in this study were the ozone mass mixing ratio, relative humidity, temperature, and cloud cover fraction. These data were selected to match the local time of the MODIS overpass and were synthetized into atmospheric profiles as input data in the MODTRAN model to produce the irradiance parameters used in this study. When both MODIS and ERA5 ozone data were unavailable, the ozone column value was set equal to the MODTRAN default value.

III. Methodology

When solar radiation passes through the Earth's atmosphere, it is modified by absorption, scattering, and reflection. The irradiance (E_{total}, W/m^2) reaching the surface through the atmosphere is usually expressed as

$$E_{\text{total}} = E_0 \cdot \cos(\theta_i) \cdot \tau \tag{1}$$

where E_0 (W/m^2) is the extraterrestrial solar irradiance and is a function of the top-of-atmosphere (TOA) solar constant and the Sun–Earth distance [see (A-1) and (A-2)]; θ_i is the solar incident angle (radian) between the normal to the slope's surface and the Sun's rays at the satellite overpass time and can be derived from the DEM; and τ (-) is the atmospheric transmittance.

The solar irradiance at the land surface consists of direct, diffuse and reflected components [16]. The atmospheric transmittance τ in (1) is influenced by multiple scattering and absorption processes in the atmosphere including: 1) uniformly mixed gas absorption; 2) Rayleigh scattering; 3) water vapor absorption; 4) ozone absorption; and 5) aerosol extinction.

Equation (1) accounts for the effect of the terrain orientation on the irradiance E_{total}, but it does not explicitly take into account other terrain effects, i.e., terrain shadows and surrounding topography. The Sun's position and the surface orientation affect the ratio of the direct to diffuse irradiance components, as well as the amount of terrain reflected radiance reaching an adjacent surface [1]. Following Sandmeier and Itten [1], SSI on a facet at a given elevation on a rugged land surface can be partitioned into four components and described as follows:

$$\begin{aligned} E_{\text{total}} &= \underbrace{\Theta E_d \frac{\cos\theta_i}{\cos\theta_s}}_{E_{dc}} + \underbrace{E_f k \frac{\cos\theta_i}{\cos\theta_s}}_{E_{\text{cir}}} + \underbrace{E_f(1-k)V_d}_{E_{\text{iso}}} \\ &\quad + \underbrace{\left(E_d + E_f\right)V_t \rho_{\text{adj}}}_{E_t} \end{aligned} \tag{2}$$

where Θ is a binary coefficient, θ_s is the solar zenith angle, E_d (W/m^2) is the direct irradiance on a horizontal surface, E_f (W/m^2) is the diffuse irradiance on a horizontal surface, V_d is the SVF, k is Hay's anisotropy index [50], V_t is the TVF, and ρ_{adj} is the surface reflectance of the adjacent objects. The four components of SSI are: 1) the solar radiation directly reaching the surface through the atmosphere (E_{dc}, W/m^2); 2) part of the radiation scattered in the atmosphere can reach the surface as diffuse irradiance (E_{iso}, W/m^2), which is a function of the proportion of the sky hemisphere not obstructed by the topography; 3) the scattering of direct sunlight in the atmosphere (E_{cir}, W/m^2), which can be modeled to account for the topography by the same method used for the direct irradiance [1]; and 4) the irradiance reflected by the terrain surrounding the target facet (E_t, W/m^2), which consists of

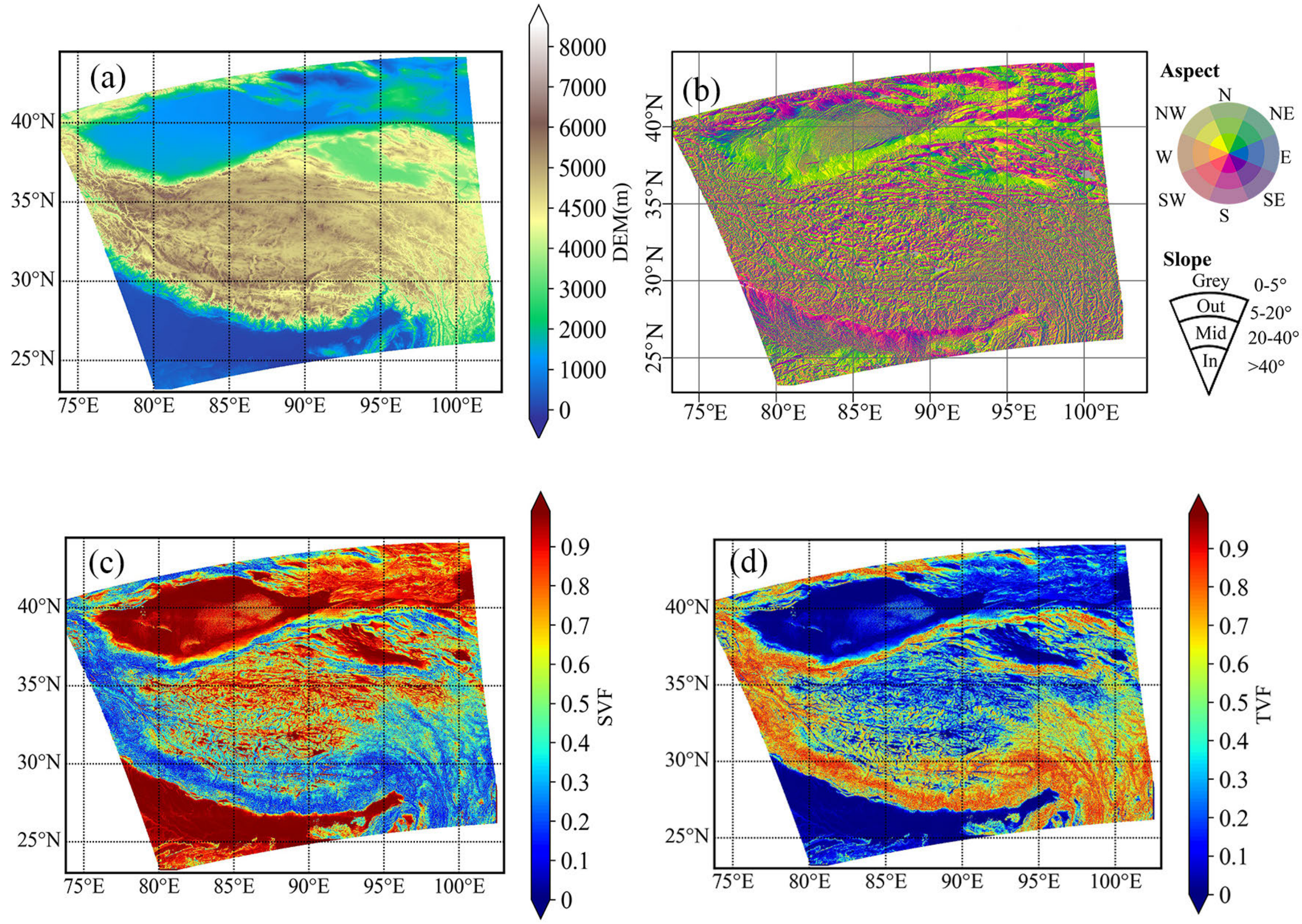

Fig. 2. (a) ASTER-GDEM2 elevation, (b) slope and aspect, (c) SVF, and (d) TVF with a 1-km resolution for the MYD 5-min Swath on 20180102:0715 in the study area.

both the direct and diffuse irradiances reflected by all the surrounding visible terrain facets [51], [52].

Two schemes can be used to estimate the clear-sky direct irradiance (E_d) and diffuse irradiance (E_f) on a flat surface in (2): 1) the parameterization scheme [(3) and (5)–(13) for E_d and (18) and (19) for E_f], which uses MODIS atmospheric data products as input to estimate the atmospheric transmittance by parameterizing the transmittances of atmospheric components and then E_d and E_f and 2) the LUT scheme, which estimates E_d and E_f directly from an LUT constructed by using a synthetic atmospheric profile generated from ERA5 reanalysis data as input to MODTRAN (see Appendix B). The parameter settings and procedures used to generate LUTs are summarized in Table V (see Appendix B for detailed description). E_d and E_f onto a horizontal surface at the MODIS overpass time are extracted from the LUT entries. The LUT scheme is used when MODIS atmospheric data are not available.

The cf from MOD06 is used to estimate the portion of each pixel that is covered by clouds. After the direct and diffuse transmittances are obtained using the parameterization or the LUT schemes, the direct and diffuse components of the irradiance on a flat surface can be computed. Finally, the SSI and its four components on a tilted surface are estimated with a 1-km resolution using the physically based model [see (2)] proposed by Sandmeier and Itten [1] to correct atmospheric and topographically induced illumination effects. The workflow used to estimate the SSI over rugged terrain is illustrated schematically in Fig. 3. The detailed methods are described in Sections III-A–III-C.

A. Direct Irradiance Under Clear and Cloudy Conditions on a Tilted Surface

In general, direct irradiance accounts for a large fraction of the SSI under clear-sky conditions. The direct solar irradiance is affected by the slope and azimuth of the target terrain facet. When solar radiation passes through the atmosphere under clear-sky conditions, part of the energy is absorbed by water vapor, part is absorbed by uniformly mixed gases, part is scattered or absorbed by aerosols, and part is absorbed by ozone [15].

The direct component of the irradiance on a horizontal surface under clear-sky conditions (E_d) is

$$E_d = E_0 \cdot \cos(\theta_s) \cdot T_B \tag{3}$$

where T_B is the direct beam transmittance. The direct irradiance measured on a facet of rugged terrain (E_{dc}) is then

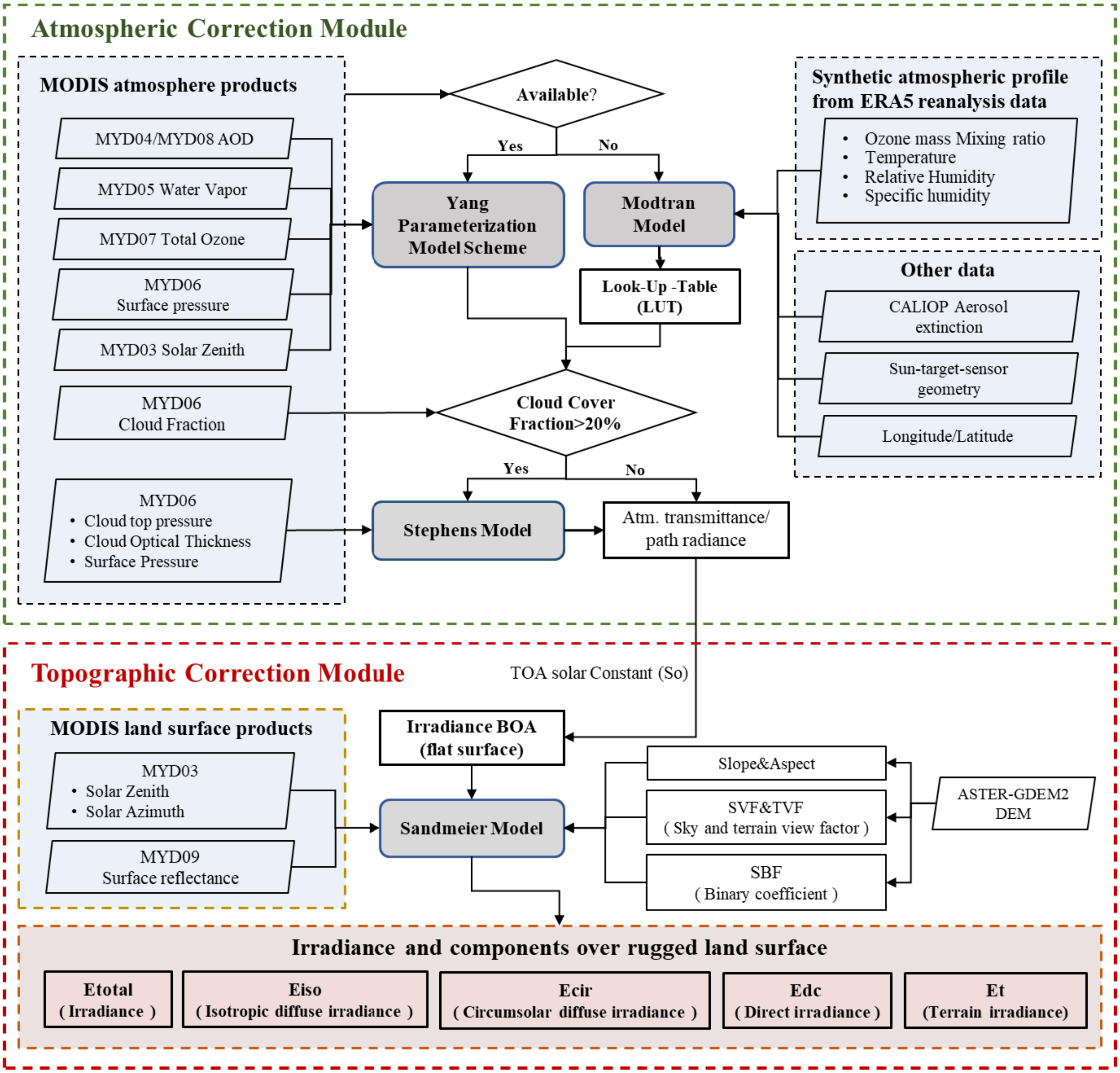

Fig. 3. Schematic of the workflow for the computation of the SSI and its four components (E_{dc}, E_{iso}, E_{cir}, and E_t) over rugged terrain.

calculated according to the cosine law to the direct irradiance E_d on a horizontal facet as follows:

$$E_{\mathrm{dc}} = \Theta \cdot E_d \frac{\cos\theta_i}{\cos\theta_s} \tag{4}$$

where Θ is a factor that takes into account the shadows cast by the terrain, with 0 for a facet in a shadow and 1 for a facet in a sunlit.

Under clear-sky conditions, the direct beam transmittance (T_B) can be divided into several components, each of which is related to a specific attenuation process with a distinct transmittance spectrum [15],.i.e., the Rayleigh scattering (τ_r), aerosol extinction (τ_a), ozone absorption (τ_o), water vapor absorption (τ_w), and permanent gases (uniformly mixed gases such as CO_2, CO, N_2O, CH_4, and O_2) absorption (τ_g). The direct beam transmittance (T_B) can then be expressed as [53]

$$T_B = \tau_r \cdot \tau_a \cdot \tau_o \cdot \tau_w \cdot \tau_g. \tag{5}$$

Following Yang [12], the broadband (spectrally integrated) transmittance functions are parameterized as follows:

$$\tau_r = \exp\Big[-0.008735\ \mathrm{ms} \cdot \big(0.547 + 0.014\ \mathrm{ms} - 0.00038\ \mathrm{ms}^2 + 4.6 \times 10^6 \mathrm{ms}^3\big)^{-4.08}\Big] \tag{6}$$

$$\tau_a = \exp\Big\{ - m \cdot \beta \cdot [(0.6777 + 0.1464\,(m \cdot \beta)] - \big[0.00626(m \cdot \beta)^2\big]^{-1.3} \Big\} \tag{7}$$

$$\tau_o = \exp\left[-0.0365 \times (m \cdot l)^{0.71136}\right] \tag{8}$$

$$\tau_w = \exp\left[-0.05 \cdot (m \cdot w)^{0.3097} - 0.0138 \cdot \ln(m \cdot w) - 0.0581\right] \tag{9}$$

$$\tau_g = \exp\left(-0.0117 \text{ ms}^{0.45}\right) \tag{10}$$

where m (-) is the relative air mass, ms (-) is the pressure-corrected relative air mass, w (cm) is the precipitable water, l (cm) is the thickness of the ozone layer, and β is the Ångström turbidity coefficient.

The air mass (m) and the pressure-corrected air mass (ms) are calculated as follows [15]:

$$m = \frac{1}{\sin a_s + 0.15(57.296 a_s + 3.885)^{-1.253}} \tag{11}$$

$$\text{ms} = m \cdot \left(\frac{P}{P_0}\right) \tag{12}$$

where P_0 is the standard atmospheric pressure at sea level (1.013×10^5 Pa), P is the actual atmospheric pressure at the target surface, which is critical in this study due to the high elevation and, thus, low pressure on the Tibetan Plateau, and a_s is the solar elevation angle.

The Ångström turbidity coefficient, β, is defined at a wavelength of $\lambda = 0.5$ μm using an Angstrom exponent of 1.3 as a function of AOD [13], [15]:

$$\beta = 0.5^{1.3}\text{AOD} = 0.406 \cdot \text{AOD}. \tag{13}$$

The input variables for the calculation of direct irradiance E_{dc} under clear-sky conditions by the model are the surface pressure, precipitable water, optical thickness of the ozone layer, ozone thickness, and AOD, which can be obtained from MODIS products (see Table II).

cf from MOD06, defined as the portion of each pixel covered by clouds, determines the impact of the clouds on the solar radiation. There is no direct radiation under full cloudy-sky conditions (cf = 100%). If the cf is less than 20%, we neglect the effect of the clouds and calculate the irradiance under clear-sky conditions. For partially cloudy conditions (20% $\leq$ cf $<$ 100%), the direct irradiance (E'_{dc}) is estimated as a proportion of clear-sky value as

$$E'_{\text{dc}} = (1 - \text{cf}) \times E_{\text{dc}}, \quad 20\% \leq \text{cf} < 100\%. \tag{14}$$

B. Diffuse Irradiance on a Tilted Surface Under Clear- and Cloudy-Sky Conditions ($\mathbf{E}_{iso}$ and $\mathbf{E}_{cir}$)

The diffuse irradiance at the surface is the energy flux density received by a surface facet after the solar radiation has been scattered by the atmospheric components in the entire sky hemisphere (below the clouds, if present). That is, the small particles and molecules that are suspended in the atmosphere scatter the sunlight in all directions, and the portion of radiation scattered toward the surface is the diffuse irradiance. For example, half of the Rayleigh scattering is scattered to the surface, while the other half is scattered back into the sky. The absorption by most aerosol particles, of which dust is found to be the most prominent aerosol type over the Tibetan Plateau [35], is so weak that their extinction is almost entirely due to scattering.

In mountainous areas, the diffuse irradiance is mainly affected by two factors: 1) the relative orientation between a surface facet and the Sun and 2) the influence of the slope and surrounding terrain on the irradiance at the target (observed) facet. The diffuse irradiance is separated into isotropic and circumsolar (anisotropic) components. In general, the diffuse irradiance is taken into account by assuming that it is isotropic, but, on a tilted facet, its anisotropic circumsolar portion should be considered.

Under clear-sky conditions, the isotropic diffuse irradiance (E_{iso}) and the anisotropic circumsolar diffuse irradiance (E_{cir}) on an inclined facet are calculated as

$$E_{\text{iso}} = E_f(1 - k)V_d \tag{15}$$

$$E_{\text{cir}} = E_f k \frac{\cos\theta_i}{\cos\theta_s} \tag{16}$$

where k is the ratio of the direct irradiance on a flat surface (E_d) to the irradiance at the top of the atmosphere (E_0), i.e., $k = E_d/E_0$. V_d is the SVF, defined as the ratio of the sky portion seen from a specific facet to that on an unobstructed horizontal facet (TVF $= 1 - V_d$). For a set of n directions, V_d is computed following the analytical algorithm developed by Zakšek et al. [54]:

$$V_d = 1 - \frac{\sum_{i=1}^{n} \sin H_i}{n} \tag{17}$$

where the horizon angle (H_i) is also referred to as the vertical elevation angle of the relief horizon, which is the largest slope angle between the horizon and any other vantage point in a given direction. V_d ranges from 0 to 1, with values close to 1 indicating flat terrain and values close to 0, indicating that the location is completely obstructed.

In (15) and (16), E_f is the diffuse component of irradiance on a horizontal surface under clear-sky conditions and is calculated as

$$E_f = E_0 \times \cos\theta_i \times T_D. \tag{18}$$

The diffuse transmittance T_D is estimated using

$$T_D = 0.5\tau_o \times \tau_w \times \tau_g \times (1 - \tau_a \tau_r). \tag{19}$$

Under cloudy conditions, the top of a cloud will reflect part of the solar radiation back into space, and part of it will reach the Earth's surface through the clouds. The diffuse and monodirectional beam irradiances are computed for the atmospheric conditions over the clouds first. The effect of the clouds is described using the parameterization method of Stephens [55] and Stephens et al. [56] to estimate the reflection, transmission, and absorption by the clouds in the two spectral regions that divide the solar shortwave range into two broad bands, i.e., 0.30–0.75 and 0.75–4 μm. This method has been applied and validated by Van Laake and Sanchez-Azofeifa [57] and Roupioz et al. [58].

Under cloudy conditions, the isotropic diffuse irradiance (E'_{iso}) in a pixel is composed of three components: the isotropic diffuse irradiance in the cloudless part, the isotropic diffuse irradiance transmitted by the clouds, and the isotropic diffuse irradiance scattered by the clouds, and E'_{iso} is written as

$$E'_{\text{iso}} = E_f(1-\text{cf})(1-k)V_d + T'_B E_0 \text{cf} \cos\theta_s V_d + (1-T_B)E_{\text{iso}}\text{cf}. \tag{20}$$

The circumsolar component of the diffuse irradiance E'_{cir} is estimated by

$$E'_{\text{cir}} = E_f(1-\text{cf})k\frac{\cos\theta_i}{\cos\theta_s} + \left(1-T'_B\right)E_{\text{cir}} \times \text{cf} \tag{21}$$

where T'_B is the total transmittance under cloudy conditions estimated by

$$T'_B = \tau'_r \times \tau'_w \times \tau'_g \times \tau_a \times \tau_o \times \tau_c \tag{22}$$

where the cloud transmittance (τ_c) is added to describe the fraction of the shortwave radiation that is not reflected by the clouds. τ_c is calculated from the optical thickness of the cloud (otc) and the backscattered fraction (δ) of the monodirectional incident radiation at the zenith angle μ_0, which is linearly interpolated from the data reported by Stephens et al. [56]

$$\tau_c = 1 - \frac{\delta(\mu_0) \times \frac{\text{otc}}{\mu_0}}{1 + \delta(\mu_0) \times \frac{\text{otc}}{\mu_0}} \tag{23}$$

where τ_c is the integrated direct beam transmittance for the two broad bands, i.e., 0.3–0.75 and 0.75–4 μm. The formulation assumes that no absorbing medium is present in the clouds.

The atmospheric water vapor is assumed to be present only below the top of the clouds. While the equations used to calculate τ_a and τ_o remain unchanged, the equations used to estimate τ'_r, τ'_g, and τ'_w are modified as follows:

$$\tau'_r \approx \exp\left(-0.008735\lambda^{-4.08}\text{mc}\right) \tag{24}$$
$$\tau'_w \approx 1 \tag{25}$$
$$\tau'_g = \exp\left(-0.0117\text{mc}^{0.3139}\right). \tag{26}$$

Under cloudy conditions, the air mass is corrected using the cloud top pressure (P_c) provided by the MYD06 product, resulting in the pressure-corrected mass of the air as

$$\text{mc} = m(P_c/P_0). \tag{27}$$

The input variables for calculation of diffuse irradiance on a tilted surface under clear-sky and cloud-sky conditions by the model are the surface pressure, precipitable water, optical thickness of the ozone layer, cloud top pressure, cf, cloud optical thickness, and AOD, which can be obtained from MODIS products (see Table II).

C. Terrain Irradiance on a Tilted Surface Under Clear and Cloudy Conditions ($\mathbf{E_t}$*)*

The terrain irradiance depends on the geometry between the position of the Sun and the orientation of the facet, which affects the total irradiance, the terrain-view factor, and the mean reflectance of the neighboring facets. The radiance reflected by the neighboring facets contributes to the irradiance at the observed facet, particularly in deep valleys. The terrain irradiance is calculated for a tilted facet under clear-sky conditions as follows:

$$E_t = \left(E_d + E_f\right)V_t\rho_{\text{adj}} \tag{28}$$

where ρ_{adj} is the surface reflectance of the adjacent objects. V_t (TVF) is defined as the portion of the overlying hemisphere obscured by the surrounding terrain and is calculated as

$$V_t = 1 - V_d. \tag{29}$$

Under cloudy skies, the terrain irradiance is calculated for a tilted facet as follows:

$$E'_t = \left(E'_{\text{dc}} + E'_f\right)V_t\rho_{\text{adj}} \tag{30}$$
$$E'_f = T'_B E_0 \cos\theta_i \times \text{cf} + (1-\text{cf})\cdot E_f. \tag{31}$$

D. Validation Approach

We used three error metrics for the evaluation: the bias (Bias), root mean square error (RMSE), and determination coefficient (R^2), which were calculated as follows:

$$\text{Bias} = \frac{1}{n}\sum_{i=1}^{n}(\text{estimated}_i - \text{observed}_i) \tag{32}$$

$$\text{Relative Bias} = \frac{1}{n}\sum_{i=1}^{n}\left[\frac{(\text{estimated}_i - \text{observed}_i)}{\text{observed}_i}\right] \times 100\% \tag{33}$$

$$\text{RMSE} = \sqrt{\frac{1}{n}\sum_{i=1}^{n}(\text{estimated}_i - \text{observed}_i)^2} \tag{34}$$

$$R^2 = \frac{\left(\sum_{i=1}^{n}\left(\text{observed}_i - \overline{\text{observed}}\right) \times \left(\text{estimated}_i - \overline{\text{estimated}}\right)\right)^2}{\sum_{i=1}^{n}\left(\text{observed}_i - \overline{\text{observed}}\right)^2 \times \left(\text{estimated}_i - \overline{\text{estimated}}\right)^2} \tag{35}$$

where estimated_i is the value estimated using the method developed in this study, observed_i is the ground observation value, $\overline{\text{estimated}}$ is the average estimated value, and $\overline{\text{observed}}$ is the average observation value. n is the number of estimates and measurements.

IV. RESULTS

We estimated the SSI and its four components taking into account the coupled effects of the topography and atmosphere at a 1-km spatial resolution on the Tibetan Plateau. The method was evaluated against in situ measurements recorded at Dali, Linzhi, MAWORS, and QOMS Stations in 2018. This validation revealed that the SSI estimates are in satisfactory agreement with the ground observations (see Section IV-A).

A. Validation of Instantaneous SSI

The method used to estimate the instantaneous SSI was evaluated against a set of ground observations at the four stations on the Tibetan Plateau in 2018 (see Table I). We used time-averaged observations with a temporal resolution of 30 min (QOMS and MAWORS) or 1 h (Linzhi and Dali).

We take the Dali Station as an example to analyze temporal patterns (see Section IV-B). The estimates were in satisfactory agreement with the ground measurements (see Fig. 4). Among the four stations, the best performance was achieved at MAWORS (see Fig. 4), with R^2, RMSE, and BIAS values of 0.61, 205.7 W/m^2, and -102.2 W/m^2, respectively. For the QOMS Station, there were few observations in March, April, and May 2018. The error metrics for Dali, Linzhi, and QOMS are given as follows: R^2 values of 0.44, 0.41, and 0.49; RMSE values of 176.9, 186.0, and 201.3 W/m^2, and BIAS values of 42.6, 59.7, and -117.7 W/m^2, respectively (see Table III).

There are currently only a few publicly available diffuse radiation observation datasets for the Tibetan Plateau. The observations of the diffuse irradiance at the Dali Station were used in this study to evaluate our retrievals of the diffuse irradiance. R^2, RMSE, and relative bias of the estimated diffuse irradiance at the Dali Station were 0.71, 94.9 W/m^2, and 31%, respectively (see Fig. 5). Notably, our diffuse irradiance estimates at the Dali Station (see Fig. 5) performed better than our SSI estimates (see Fig. 4).

B. Time Series of SSI and Its Components

Based on the methodology described in Section III and using the required data (see Section II), a time series of the instantaneous SSI and its four components with a 1-km spatial resolution in 2018 were produced. An example of the Dali Station (see Table I) in 2018 is shown in Fig. 6, where the time series of the estimated instantaneous SSI, observed instantaneous SSI, estimated direct irradiance, estimated isotropic diffuse irradiance, estimated circumsolar diffuse irradiance, and estimated terrain irradiance are plotted. The instantaneous SSI was estimated at the MODIS (Aqua satellite) overpass time, i.e., between 12:00 and 13:30 P.M. local time at the Dali Station. The SSI, direct, isotropic diffuse, and terrain irradiances showed significant seasonal variability on clear days. As was expected, the clouds had a large impact on the direct radiation.

The trends of AOD, E_{cir}, and E_{iso} were basically the same under clear skies (see Fig. 6). With the appearance of clouds and the increase in the cf, the diffuse radiation increased accordingly, especially E_{iso}.

Regarding the evaluation of our estimates of the diffuse irradiance, observations were only available at the Dali Station. The annual average instantaneous AOD was 0.15 at the MODIS overpass time at the Dali Station. The AOD increased from March to May [see Fig. 6(d)]. The statistics showed that the annual average of the instantaneous estimated E_{iso} was 226.1 W/m^2 in 2018, while E_{cir} was 46.3 W/m^2. E_{iso} and E_{cir} accounted for 37.57% and 7.68% of the total annual SSI in 2018, respectively, indicating that diffuse irradiance accounted for a large proportion throughout the entire year.

The annual maximum diffuse irradiance occurred in April ($E_{\text{iso}} = 197.2$ W/m^2 and $E_{\text{cir}} = 93.4$ W/m^2) when AOD had the highest value of the year (0.76) and cloud cover was 22%. This may be due to biomass combustion in southern Asia, which results in an increased aerosol concentration over the Tibetan Plateau [59], [60], [61]. From March to May, the mean daily cloud cover was 56.4%, with 20 clear-sky days. The fluctuations in E_{cir} and E_{iso} were consistent with the fluctuations in the AOD. Under cloudy conditions, E_{iso} was not only affected by aerosols but also by the clouds (see Fig. 7). In particular, the strong surface heating made the air stratification very unstable and produced deep air convection from June to August, leading to a higher degree of cloud cover. In June, the cf was often high (close to 100%), and the otcs were less than 10, in which case the contribution of E_{iso} to SSI was the largest. In the model of Stephens et al. [56] used in this study, it is assumed that the clouds are liquid water clouds, assuming that the wrong cloud type leads to less accurate estimates.

C. Comparison With the MCD18A1 and ERA5 SSI Data Products

To further evaluate the reliability of our SSI estimation, the MODIS instantaneous SSI data product (MCD18A1) and the ERA5 hourly SSI data product were selected for comparison with the same in situ observations used to evaluate our SSI estimates. The spatial resolutions of the MCD18A1 and ERA5 SSI data products are 1 and 25 km, respectively. This comparison further emphasized the potential improvements with our proposed method (see Table III and Figs. A-I and A-II). For the MCD18A1 instantaneous SSI data, the observations at the MAWORS Station showed the best performance with an R^2 of 0.38, RMSE of 243.1 W/m^2, and BIAS of -26.2 W/m^2. The other stations had lower R^2 values and higher RMSE and BIAS values, indicating variability in performance across locations. The ERA5 hourly SSI data showed better performance at MAWORS with R^2 of 0.44, RMSE of 230.6 W/m^2, and BIAS of 106 W/m^2. The performance metrics at the other stations also indicated a reasonable agreement with ground observations (see Fig. A-II). Our proposed estimation methods showed a better agreement with ground measurements, particularly at MAWORS with R^2 of 0.61, RMSE of 205.7 W/m^2, and BIAS of -102.2 W/m^2. The error metrics for the other stations also demonstrated improvements over the existing satellite and reanalysis datasets. The larger dispersion in the scatter plots for MCD18A1 and ERA5 may be due to not accounting for terrain effects. This dispersion underscores the potential for these methods to yield less reliable results under diverse terrain conditions. The superior error metrics at the Linzhi site compared with MCD18A1 and ERA5 products, despite its high cloud cover, may indeed highlight the robustness of our method, particularly on cloudy days.

D. Effects of Aerosols and Cloud Cover on Diffuse Irradiance

To evaluate the effect of clear- and cloudy-sky conditions, the estimated and measured instantaneous diffuse irradiances were compared for different cfs to evaluate whether the differences were significant (see Fig. 8). As was expected, the best agreement was obtained for clear-sky conditions (cf $< 20\%$). As the cf increased, the difference between the estimated and observed diffuse irradiances increased slightly, i.e., the uncertainty of the estimates increased (see Table IV).

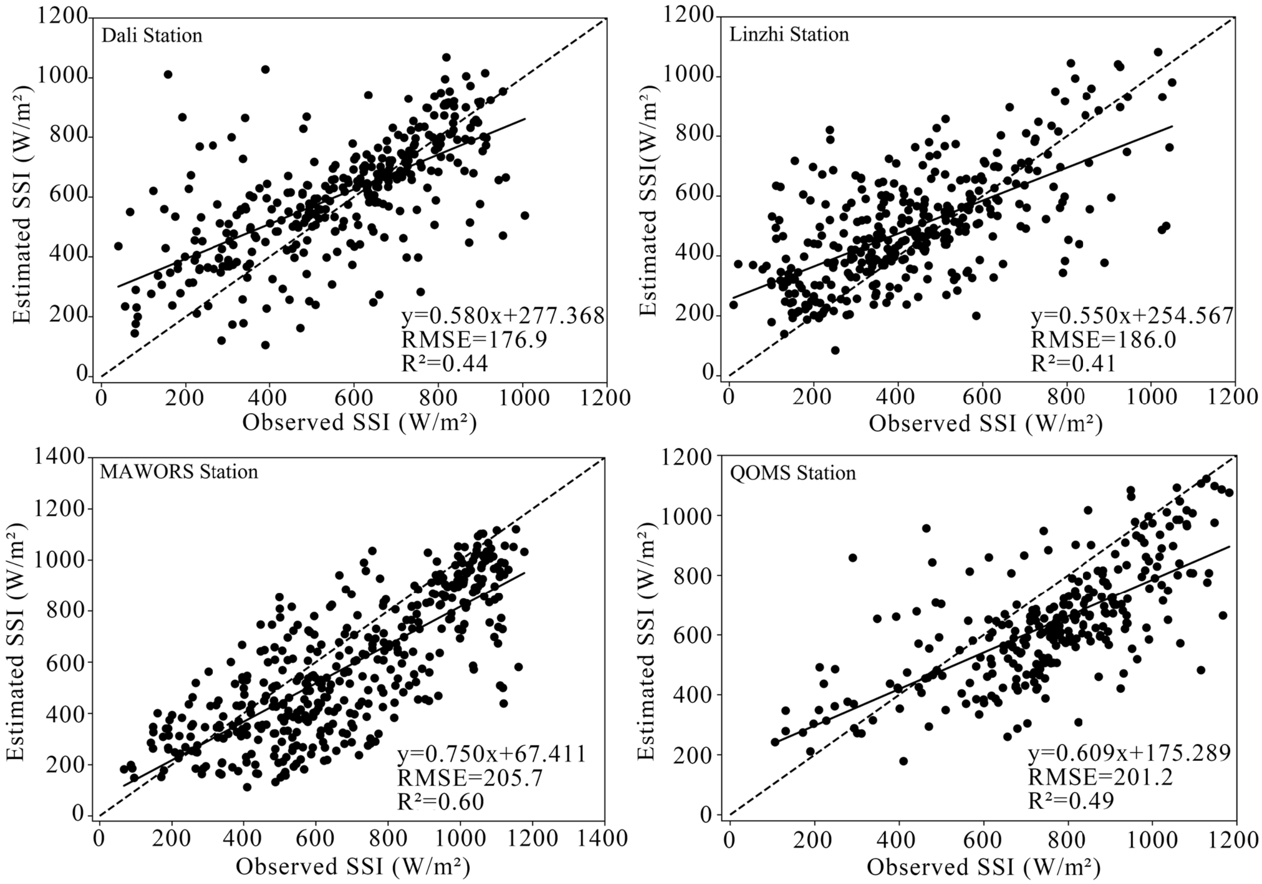

Fig. 4. Validation of the instantaneous SSI estimated using the method developed in this study compared to observations at Dali, Linzhi, MAWORS, and QOMS Stations in 2018 during the MODIS Aqua overpass time.

TABLE III
COMPARISON SSI WITH MCD18A1 AND ERA5 SSI PRODUCTS

Metrics	Dali			Linzhi			MAWORS			QOMS		
	Our method	MCD18A1	ERA5	Our method	MCD18A1	ERA5	Our method	MCD18A1	ERA5	Our method	MCD18A1	ERA5
R^2	0.44	0.19	0.18	0.41	0.14	0.21	0.61	0.38	0.44	0.49	0.26	0.23
RMSE (W/m^2)	176.9	257.4	211.9	186.0	310.4	291.3	205.7	243.1	230.6	201.2	233.7	192.0
Bias (W/m^2)	42.6	-3.01	28.29	59.67	168.9	209.4	−102.2	26.2	106	−117.7	-11.9	6.3

TABLE IV
PERFORMANCE METRICS FOR THE OBSERVED VERSUS ESTIMATED INSTANTANEOUS DIFFUSE IRRADIANCES AT THE DALI STATION FOR DIFFERENT CFS

Metrics	$0\% \leq CF < 20\%$	$20\% < CF \leq 50\%$	$0\% < CF < 100\%$	$CF = 100\%$
R^2	0.52	0.41	0.41	0.41
RMSE	28.67	78.07	115.86	161.85
Bias	15.23	41.92	53.84	−58.62

The results for the nearly cloud-free conditions clearly demonstrated the impact of the aerosols on the diffuse irradiance, and every 0.1 increase in the AOD caused approximately a 35-W/m^2 increase in the total diffuse irradiance and the isotropic diffuse irradiance [see Fig. 7(a)]. At higher cfs, the estimated isotropic diffuse irradiance and the total diffuse irradiance were less sensitive to the AOD because the effect of the cf became dominant [see Fig. 7(b) and (c)].

E. Comparison of $\mathbf{E_d}$ *and* $\mathbf{E_f}$ *Estimated Using the Parameterization Scheme and LUT*

The method that we developed in this study used either MODIS data products or ERA5 data to characterize the atmospheric conditions. The impact of a limited number of MODIS atmospheric retrievals could be mitigated by applying an LUT generated using MODTRAN and ERA5 reanalysis data to fill the gaps in the time series of the observations by MODIS. In several studies [28], [49], missing values were replaced with weekly or monthly averages or default values, especially for the AOD, which is the variable with the highest rate of missing data (see Table VI). Because of its high elevation, the atmosphere on the Tibetan Plateau is thin and clear, but particles originating from both sandstorms in the Gobi area and biomass burning in southern Asia are likely to be transported to the Tibetan Plateau, which results in a higher aerosol loading.

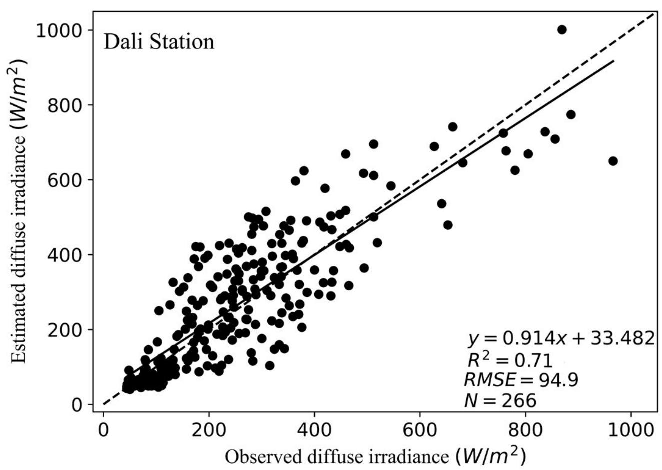

Fig. 5. Estimated versus observed diffuse instantaneous irradiance; irradiance estimated using the method developed in this study at the Dali Station at the MODIS Aqua overpass time in 2018.

TABLE V
MODTRAN PARAMETERS AND OPTIONS SET FOR THE LUT SCHEME

Parameter	Set in MODTRAN	Number of options
Atmospheric profile	ERA5 data	365
Ground altitude	0.25 km, 1 km, 2.25 km, 3.75 km, 5 km	5
Day of year	365	365
Latitude of observer	20–40° (1° increment)	20
Longitude of observer	65–110° (1° increment)	45
Green decimal hour	8	1
Surface reflectance	0.5 or 1	2
Number of combinations		3285000

TABLE VI
PERCENTAGE OF MISSING DATA FOR THE ATMOSPHERIC MYD08_D3 PRODUCTS FOR THE TIBETAN PLATEAU DURING 2012–2016

Variable	Jan	Feb	Mar	Apr	May	Jun	Jul	Aug	Sept	Oct	Nov	Dec
Precipitable water (%)	5.9	7.2	7.02	10.5	11.5	15.7	19.9	14.2	11.4	6.0	3.1	4.1
Total ozone (%)	1.7	2.4	2.1	3.8	5.4	11.5	16.7	11.9	8.6	3.7	1.1	1.5
AOD (%)	74.9	73.4	72.3	74.4	68.9	65.5	64.2	57.0	56.4	58.3	64.4	72.1

The parameterization scheme and the LUT scheme use different types of atmospheric data to estimate the direct and diffuse irradiances, and the results could be compared when the required MODIS data were available. The differences in the estimates of the direct and diffuse irradiances were found to be small but observable (see Fig. 9). Overall, the two schemes provided comparable estimates of the direct and diffuse irradiances on the Tibet Plateau even though the LUT estimates of the direct irradiance were often slightly lower than those obtained using the parameterized transmittance and MODIS data products. The parameterization scheme using instantaneous MODIS retrievals resulted in larger fluctuations in the estimated direct irradiance and diffuse irradiance than the LUT scheme using ERA5 hourly averages (see Fig. 9). Differences in the estimated diffuse irradiance were sometimes large at QOMS, with the LUT estimates being slightly higher. Most of the time, the two schemes produced comparable estimates, thus supporting the use of the LUT method to fill the gaps in the time series from the parameterization scheme using MODIS retrievals.

F. Contribution of Terrain Irradiance to SSI

The terrain irradiance is determined by several factors: the total irradiance impacting the surrounding pixels, the extent and distance of visible neighboring terrain, and the surface reflectance of adjacent pixels. We estimated the terrain irradiance for three subsets, i.e., applying to flat, gentle, and rugged terrain (see Fig. 10). Flat terrain was defined as having slope $< 5\%$, gentle with $5\% <$ slope $< 20\%$, and rugged with slope $\geq 20\%$. Each subset included 1000 randomly selected pixels over the Tibetan Plateau at the MODIS Aqua overpass time. The terrain irradiance was calculated over the eight nearest neighbors of each selected pixel. If terrain effects would not be taken into account, the results for flat terrain would apply to any terrain. Especially for rugged terrain, the terrain irradiance accounts for a rather larger fraction of SSI (see Fig. 10), increasing with increasing diffuse irradiance (see Fig. 10). The spatial variability in E_t also increases when comparing flat with rugged terrain. It should be noted that neglecting terrain effects would lead to (large) underestimation of SSI (see Fig. 10). Neglecting terrain considerations could result in errors as high as 500 W/m^2 in extreme topographic settings with specific combinations of slope and azimuth values.

We also took into account the angular distribution of the difference in SSI between a horizontal surface facet and a rugged surface facet (see Fig. 11). The difference between our estimated SSI onto a horizontal surface facet and estimated SSI onto a rugged surface facet can reach up to $\pm$600 W/m^2 in some extreme topographic configurations with large slope or azimuth values.

V. DISCUSSION

A. Overall Evaluation of Results

Estimating the SSI and its four components is of great significance for water and energy cycle research and ecosystem applications. This article proposes a practical framework for estimating the all-sky SSI and its four components, especially for rugged terrain at a 1-km resolution based on multiple remote sensing observations and reanalysis of meteorological data. The framework mainly includes two modeling/retrieval modules. The first module is used to estimate the transmittance/path radiance and cloud transmittance, in which multiple aspects of the radiance attenuation processes, including Rayleigh scattering, aerosol extinction, ozone absorption, water vapor absorption, permanent gas absorption, and cloud scattering and absorption, are carefully treated. The atmospheric conditions are extracted from remote sensing observations and reanalysis meteorological data (MODIS, CALIOP, and ERA5 data) rather than adopting climatological values as has been frequently done in previous studies such

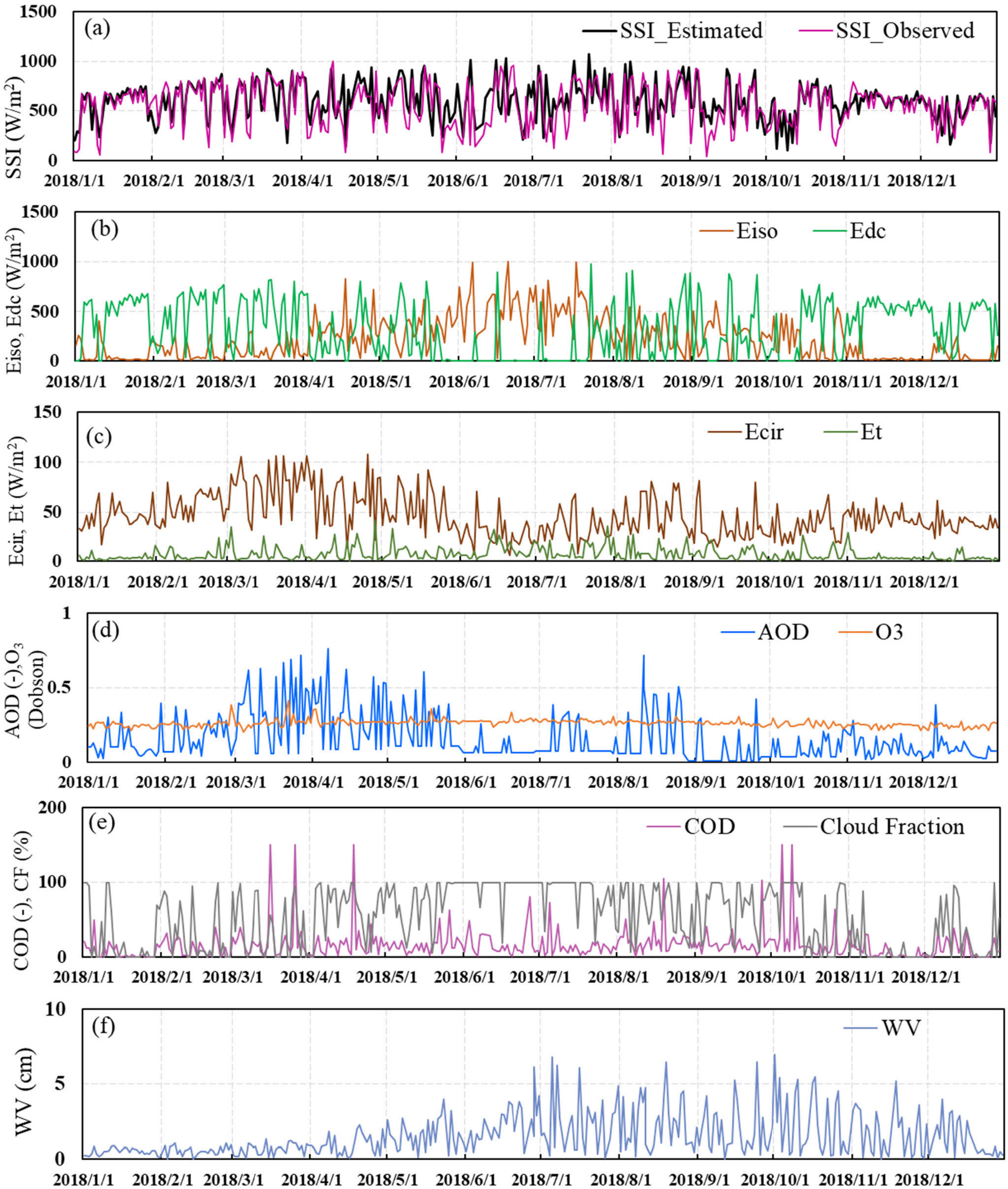

Fig. 6. (a) Estimated instantaneous SSI and observed instantaneous SSI, (b) estimated direct irradiance and estimated isotropic diffuse irradiance, (c) estimated circumsolar diffuse irradiance and estimated surrounding terrain irradiance, (d) atmospheric AOD and ozone, (e) optical thickness of clouds (COD) and cf, and (f) precipitable water vapor at the Dali site during the MODIS Aqua overpass time in 2018.

as those by Tang et al. [34] and Van Laake and Sanchez-Azofeifa [57]. This makes the atmospheric transmittance/path radiance and cloud transmittance estimation more reliable for specific applications on the Tibetan Plateau, which has unique aerosol composition and distribution characteristics [38], [36]. In addition, the combined use of parameterization and LUT methods enables the attainment of all-sky estimations, which is significant for applications on the Tibetan Plateau where serious data gaps are common. The results obtained by applying the parameterization and LUT methods show good

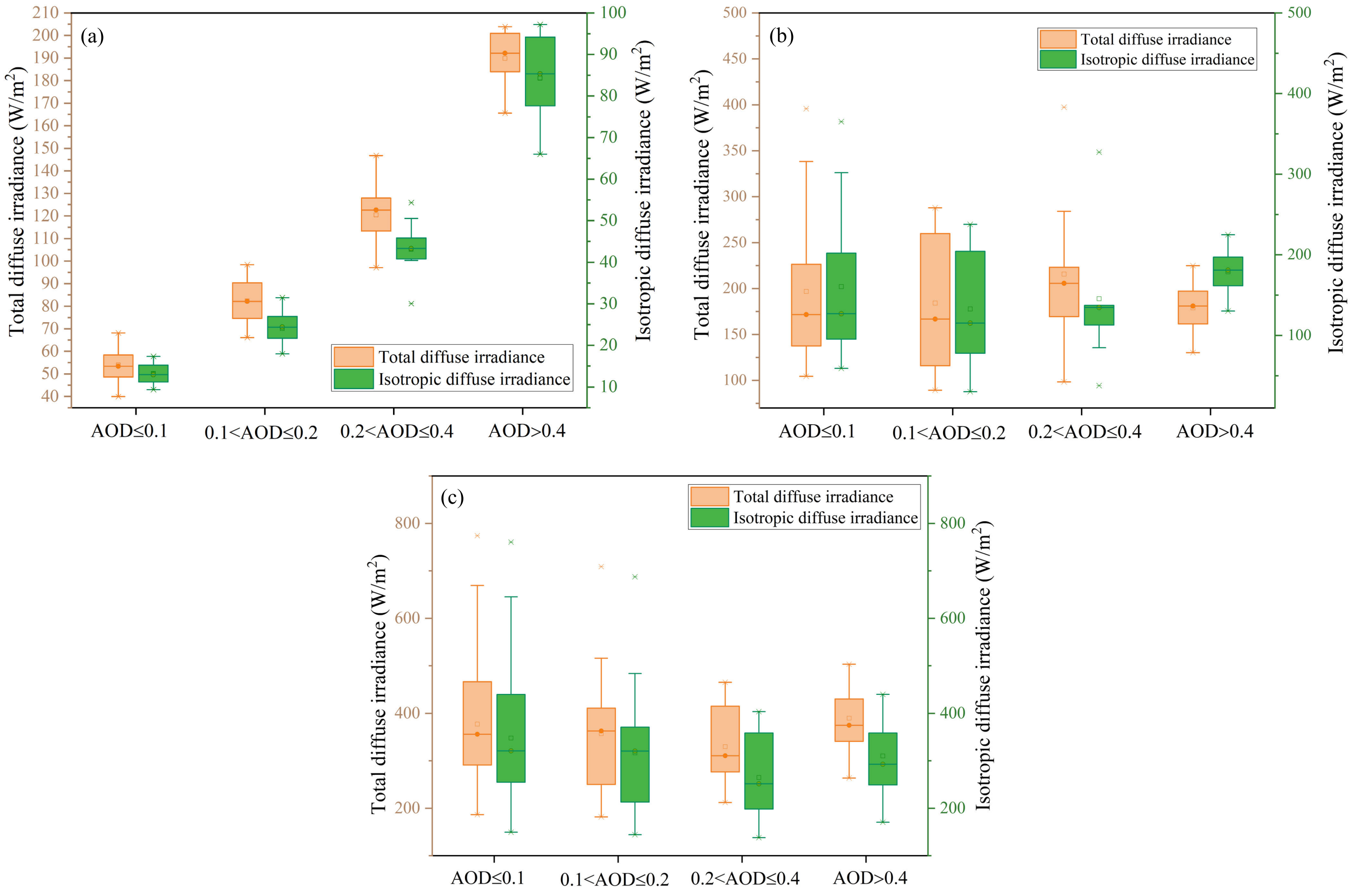

Fig. 7. Instantaneous estimates of the total diffuse and isotropic diffuse irradiance binned in four AOD ranges (i.e., AOD $\leq$ 0.1, 0.1 $<$ AOD $\leq$ 0.2, 0.2 $<$ AOD $\leq$ 0.4, and AOD $>$ 0.4) at the Dali Station during the MODIS Aqua overpass time in 2018 for (a) 0% $\leq$ cf $<$ 20%, (b) 20% $\leq$ cf $<$ 50%, and (c) 50% $\leq$ cf $<$ 100%.

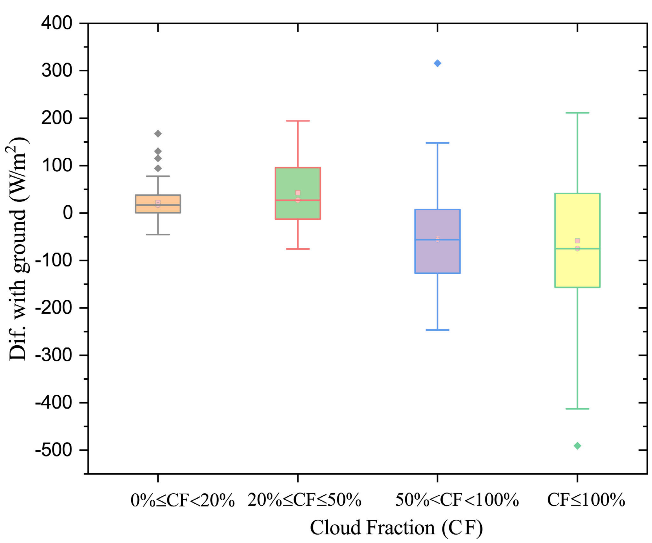

Fig. 8. Difference between observed and estimated instantaneous diffuse irradiance at the Dali Station during the MODIS Aqua overpass time in 2018 under different cfs.

consistency, which guarantees the robustness of the method when applied in a large region with diverse data availability. The other module is designed for topographic correction, and it considers the topographic influences on both the direct and diffuse irradiances, making the method more suitable for rugged surfaces such as those on the Tibetan Plateau.

Roupioz et al. [58] developed a method to produce a time series (2008–2010) of instantaneous SSI and daily solar radiative fluxes using multiple land surface and atmospheric MODIS data products combined with a DEM to take into account the actual illumination angle. We have compared our results on estimated irradiance at three sites with those of Roupioz et al. [58], who reported RMSEs ranging from 117.1.8 to 225.5 W/m^2 and R^2 ranging from 0.27 to 0.55 for all skies. As the sample size of Roupioz et al. [58] was larger than ours, the dispersion was smaller, and the mean of the distribution was closer to the population mean (central limit theorem). Thus, the sample size is negatively correlated with the standard error of a sample. The validation of SSI estimates obtained using our method against ground observations yielded RMSEs ranging from 177 to 206 W/m^2 and R^2 values ranging from 0.43 to 0.61. Overall, the results obtained for the Tibetan Plateau using the proposed method seem better than the results of Roupioz et al. [58], especially the R^2 values. This accuracy is comparable with or even better than those reported for existing algorithms [58], [62], [63].

For the SSI, the accuracy increases with decreasing cf and AOD, and a better SSI was obtained for clear skies, as expected (see Fig. 8). The evaluation of the SSI on the Tibetan Plateau revealed significant seasonal variability,

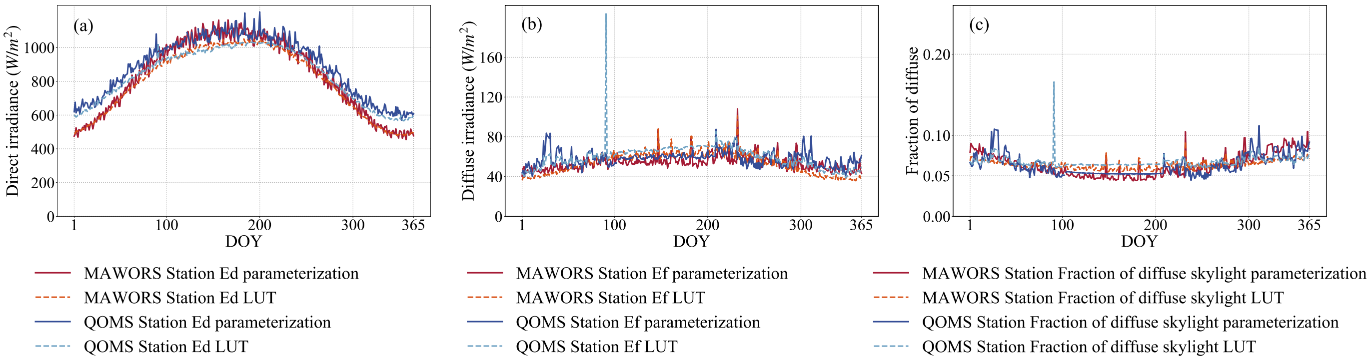

Fig. 9. Comparison of irradiance estimates by the parameterization method based on MODIS data and the LUT based on ERA5 data for a flat surface at MAWORS and QOMS: (a) direct irradiance, (b) diffuse irradiance, and (c) fraction of diffuse irradiance.

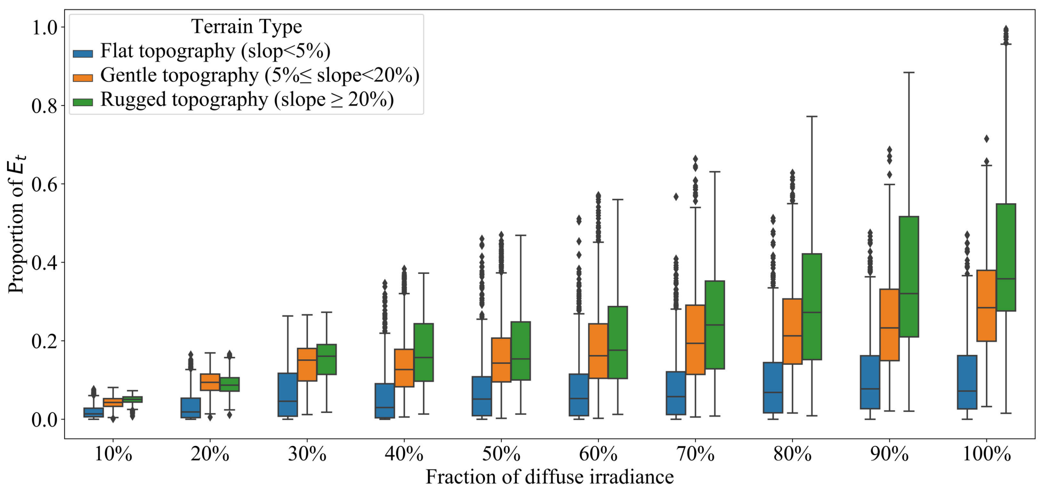

Fig. 10. Ratio of E_t to SSI at different fractions of diffuse irradiance by topography types: flat (blue), gentle (orange), and rugged (green).

specifically of the direct, isotropic diffuse, and terrain irradiances. The diffuse irradiance was found to account for a large fraction of SSI throughout the entire year, with the annual maximum diffuse irradiance occurring in April at the Dali Station. The fluctuations in E_{cir} and E_{iso} were consistent with the variations in AOD, with every 0.1 increase in AOD causing approximately a 35-W/m^2 increase in total diffuse irradiance and a decrease of about 25 W/m^2 in the total SSI under clear skies at the Dali Station and the MODIS Aqua overpass time. However, at higher cfs, the estimated E_{iso} and total diffuse irradiances were less sensitive to the AOD because the effect of the cf became dominant. The average cloud cover of the four stations, Dali, Linzhi, MAWORS, and QOMS, was 53.9%, 71.6%, 61.0%, and 38.3%, respectively, and the estimated total radiation agreed well with the ground measurement results (see Table III), so the algorithm is suitable for cloudy conditions.

The study applied two schemes in the first module to estimate SSI: one is based on the parameterization of atmospheric transmittance and the other is based on the LUT method. The study found that the two methods produced comparable estimates for direct and diffuse irradiances, particularly under clear-sky conditions. However, the LUT estimates for diffuse irradiance were sometimes slightly higher than the estimates based on the parameterization method, while the LUT estimates of direct irradiance were sometimes slightly lower than the ones based on parameterized transmittance.

B. Using the Reference Ozone and Water Vapor Profiles in MODTRAN

In many studies (e.g., [19], [64], [65]), the variability in the absorption by ozone and other gases was neglected, and the default (reference) profiles were applied in the radiative transfer calculations. Ozone has a distinct absorption band at 550–650 nm, and the variability in the amount of O_3 has an observable impact on the SSI. Although the estimated absorption by ozone is only approximately 25 W/m^2, after spectral integration in the shortwave range, it cannot be ignored.

In the case of insufficient availability of MODIS retrievals of the atmospheric properties, the alternative scheme for estimating the SSI and its components is to use ERA5 reanalysis data to generate atmospheric profiles suitable for MODTRAN calculations. In principle, this approach can capture the atmospheric conditions and yield accurate estimates of the atmospheric scattering. In some cases, the differences between the reference atmospheres and the ERA5 data are significant, such as in the case of O_3 (see Fig. 12). Three geographical–seasonal reference atmospheres were applied in MODTRAN, i.e., the 1976 U.S. standard atmosphere, the

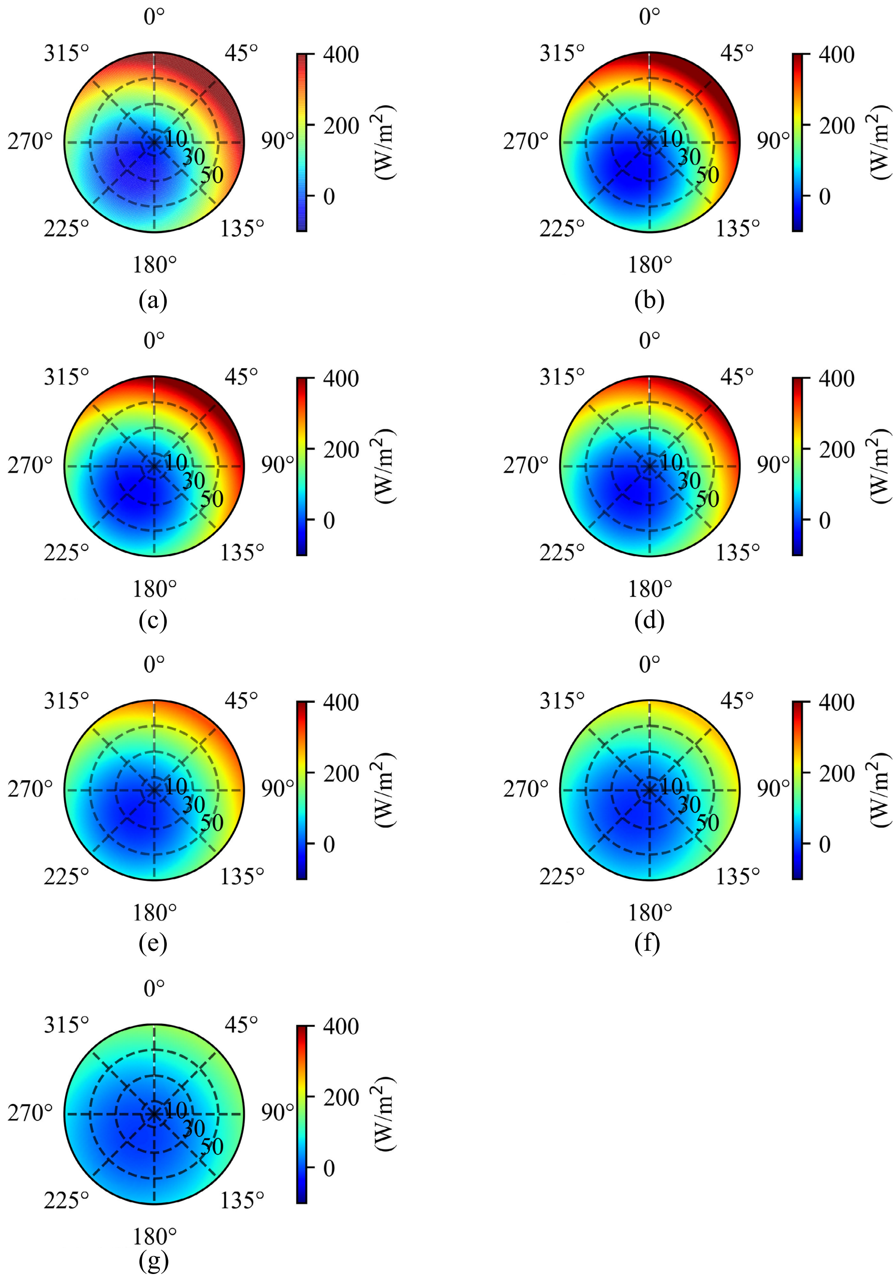

Fig. 11. Angular distribution of the difference in SSI between a horizontal surface facet and a rugged surface facet; solar zenith angle = 22.15°, solar azimuth angle = −145.11°, and sensor zenith angle = 10° for different AOD (at 0.55 μm) on January 2, 2018. The target center represents the surface slope α, β = (0°, 0°), the radial distance from the center represents the surface slope angle, and the angular distance from N represents the terrain azimuth. (a) AOD = 0. (b) AOD = 0.25. (c) AOD = 0.5. (d) AOD = 1. (e) AOD = 2. (f) AOD = 3. (g) AOD = 5.

mid-latitude summer (MS) atmosphere, and the mid-latitude winter (MW) atmosphere. These atmospheres were compared (see Fig. 12) with the ERA5 monthly averaged data at the reference pressure levels. From 10 to 22 km, the ozone concentration is very low according to the ERA5 monthly averaged data, while it is higher according to the MODTRAN standard atmospheres. The concentration of ozone initially increases and then decreases with increasing height. Zhou et al. [66] used the Total Ozone Mapping Spectrometer (TOMS) ozone data to reveal the presence of comparatively less ozone over the Tibetan Plateau, the so-called ozone valley, from June through September. One process that attenuates the radiance is absorption in the visible part of the spectrum, which is mostly due to aerosols and ozone. Overestimation of the ozone concentration by using the MODTRAN standard atmospheres can result in a bias of about 20 W/m^2 in the estimated SSI. Therefore, the irradiance can be estimated more accurately if information on the local dynamic ozone concentration, which is captured by the ERA5 hourly data at the reference pressure levels, is used to construct the atmospheric profiles.

The precipitable water vapor was assumed to be constant in some previous studies [57], [67]. Unlike O_3, the vertical profiles of the water vapor concentration for the MODTRAN mid-latitude atmosphere and in the ERA5 monthly averaged

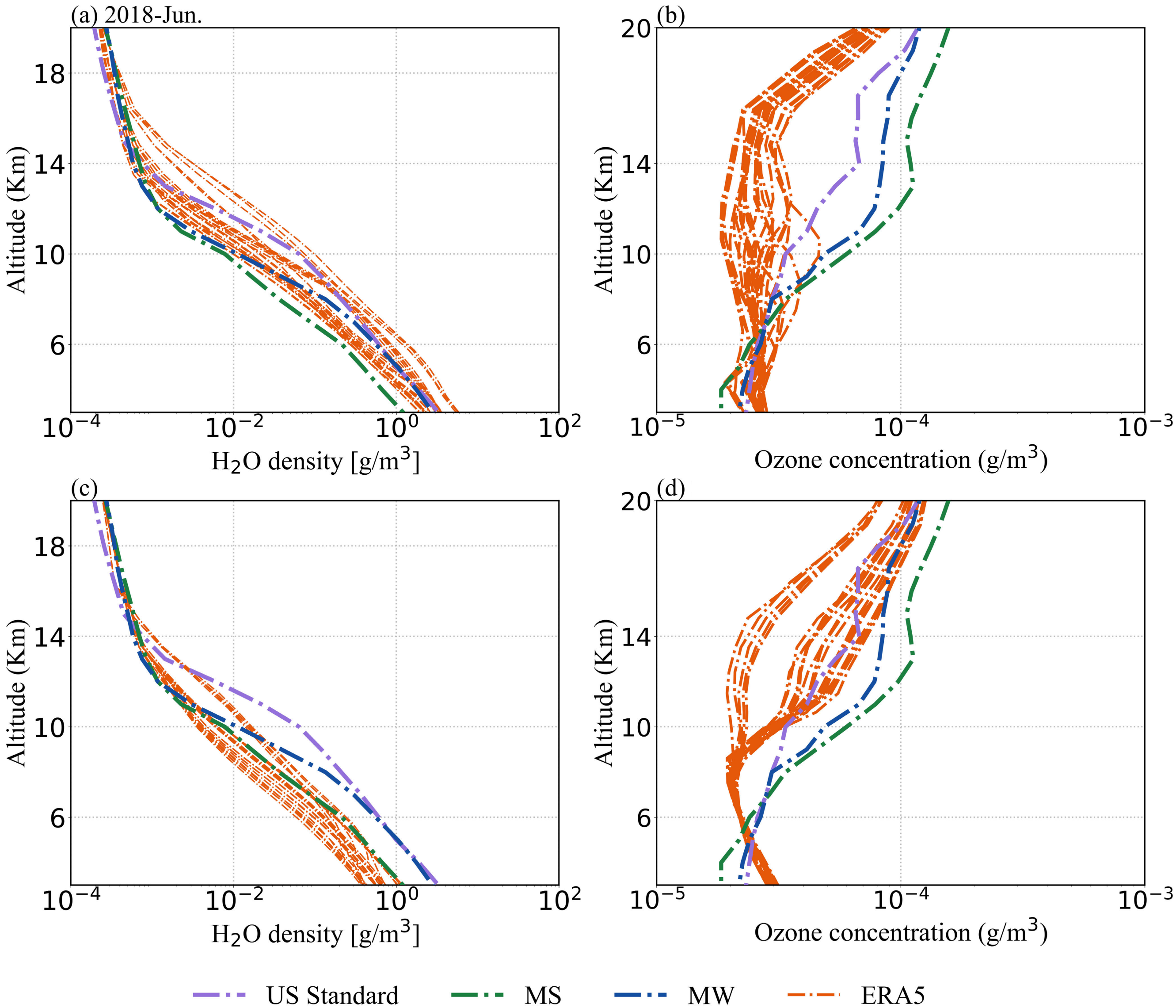

Fig. 12. Vertical profiles (from 3 to 22 km) of the ozone concentration and water vapor for the three MODTRAN model atmospheres and the ERA5 data for several randomly chosen locations on the Tibetan Plateau in June and December of 2018 at MODIS overpass time (local time: 1:30 P.M.). (a) and (b) June 2018. (c) and (d) December 2018.

data appeared to be rather similar (see Fig. 12). However, the values of the 1976 U.S. standard atmosphere profiles were higher than the synthetic atmospheric profiles obtained using the ERA5 reanalysis data for 0–14 km in winter and spring (see Fig. 12). This result suggests that it is necessary to construct a local atmospheric profile to improve the accuracy of the radiative transfer calculations.

C. Evaluation Against Ground-Based Measurements

Radiometers to measure radiative fluxes at the land–atmosphere interface are typically installed horizontally on flat terrain, which means that the field-measured SSI applies to a flat and horizontal plane. These conditions apply to the radiometers installed at our four stations (i.e., QOMS, MAWORS, Linzhi, and Dali; see Table I), where the slopes are about 5° or less (see Table I). On the other hand, our estimates of SSI apply to the plane parallel to a 1 × 1 km terrain facet. The retrieval of SSI and its four components are based on the mean slope and aspect of the terrain within each 1 × 1 km grid, determined by averaging slope and aspect calculated at a 30 × 30 m spatial resolution within each grid. If this facet has the same orientation as the terrain at the location of the radiometer used to measure SSI, the terrain geometry of our retrievals and in situ measurements should be comparable. The footprint of an in situ radiometer, however, is much smaller than the 1 × 1 km pixel applied in our retrieval. This article gave the slope and aspect values in Table I for the four observatories. At the Dali Station, the terrain orientation of the 1 × 1 km grid is comparable with the orientation at the location of the radiometer. Differences are larger for the other observatories, especially at MAWORS and Linzhi. The results of the comparison (see Fig. 4) show that the RMSE was largest at the MAWORS Station. This mismatch may have had an impact on the evaluation of our retrievals, both directly due to such mismatch and indirectly because of the influence of terrain irradiance on in situ total SSI, as suggested by the large scatter of data points in Fig. 4. To further support the interpretation of the comparison of our retrievals with in situ measurements, we have provided additional information on the terrain characteristics at each station. The QOMS is located at 4298 m.a.s.l. and 30 km from the northern boundary of Mount Everest, and it is dominated by the alpine Gobi desert with relatively flat open terrain, mainly bare ground and sparse and short vegetation. MAWORS is located close to Muztagh Mountain and Karakuli Lake and lies at 3668 m.a.s.l. The Linzhi Station is located at 2991 m.a.s.l. in a valley with relatively flat terrain. The surface is a plateau meadow surrounded by trees, and the vegetation has good growing conditions. Overall, there is a satisfactory agreement between our estimates and the in situ measurements of SSI.

D. Limitations of Our Method

In our method to estimate the SSI and its four components in the presence of clouds, we assume that within a pixel cf, the cloud cover is homogeneous, uniform, plane-parallel, and stationary. The error introduced can be significant, depending on the cloud type and the actual distribution of clouds within the entire pixel. Some researchers have found that the shape of a cloud affects diffuse radiation, and cirrostratus clouds scatter more radiation than cumulus clouds [68], [69], [70], [71], [72]. Clouds influence the partitioning of direct and diffuse radiations [73]. Clouds diffuse direct solar radiation, yielding diffuse radiation [74]. Dense clouds (such as stratocumulus clouds) reflect the incoming solar radiation and absorb most of the direct radiation [75], so little diffuse radiation reaches the surface. Below optically thin clouds (such as cirrus clouds), the diffuse radiation is greatly enhanced [74]. The type of cloud is not considered in our method, which will also reduce the accuracy of the estimates. The presence of thin cirrus clouds, even in small amounts, can significantly affect AOD retrieval. This is corroborated by Qiu [76] who highlighted the challenges in separating cloud effects from AOD measurements and the necessity of considering even minimal cloud cover in AOD estimations. Our approach might have oversimplified the impact of cloud cover on AOD retrieval. The presence of thin cirrus clouds, even when the cf is low, can lead to significant errors in AOD measurements. This aspect was not adequately addressed in our initial assumptions. In our future studies, we plan to explore ways to account for the impact of thin cirrus clouds on AOD retrieval, particularly under low cloud cover conditions. The simplification of applying a plane-parallel cloud configuration in this study to describe radiative transfer in the atmosphere is frequently used, and a detailed treatment of radiative transfer in a plane-parallel atmosphere can be found in [77]. Under clear-sky and fully cloudy conditions, the plane-parallel configuration is a realistic representation of actual atmospheric conditions. The effect of the spatial 3-D organization of fragmented clouds on the diffuse and direct irradiances was studied by Roupioz et al. [78] in a study that led to the work described here. Daytime hemispherical images were collected at a very high frequency, simultaneously with ground measurements of solar radiation fluxes at the observatory located on the shore of Namco Lake [78]. Their results show that the SSI is poorly correlated with the cf, and the cloud spatial (3)-D) distribution should be used instead as a predictor of SSI. A thorough study of the impacts of the spatial organizations of clouds on estimated radiative fluxes at the surface would require a combination of 3-D models of radiative transfer in the atmosphere and extended experiments such as the one carried out by Roupioz et al. [78]. To mitigate the impact of estimated cf on our retrievals of SSI, we calculated SSI and its components separately for the clear- and cloudy-sky fractions, i.e., we did not use directly the cf to predict SSI.

In this study, the cloud effect to calculate the SSI was neglected when cf was less than 20%. This may indeed have some impact on the accuracy of estimating SSI, and in some specific weather conditions, it may not be accurate. However, in practical applications, the estimation of shortwave solar irradiance often requires a tradeoff between accuracy and computational complexity. If there is a small amount of cloud cover, ignoring the radiative effects of clouds can simplify the calculation process and may have a small impact on the results in some applications. We rely on Damiani et al.'s [79] study, which demonstrates that clear-sky conditions were observed up to a cf of approximately 20% when the clear-sky index was equal to 1. When the cf is lower than 20%, the estimation of atmospheric transmittance is done by (5) as clear-sky conditions. When estimating solar irradiance, cloud effects should be considered as much as possible, and appropriate processing should be performed based on actual conditions to ensure the accuracy and reliability of the results.

The retrieval of aerosol properties from measurements of the spectral upwelling TOA radiance by space-borne imaging radiometers such as MODIS is particularly challenging under conditions of low aerosol load, low atmospheric optical thickness, and over bright land targets, which are widespread on the Tibetan Plateau. Previous studies by our team [80], [81], [82], [83], however, did show that it is possible to improve AOD retrieval with MODIS data under such conditions by improving the characterization of background radiance and the vertical distribution of aerosols. The results described in these references [80], [81], [82], [83], document improvements in the frequency of valid retrievals and in their accuracy. The workflow developed by Wu et al. is one of the two components of the system developed in our follow-up research. The other major component is the workflow developed by Roupioz et al. [33], [58], [78] to improve the retrieval of surface reflectance by improving the retrieval of SSI and surface bidirectional reflectance distribution function (BRDF), also with MODIS data. Our study is based on the integration of these two workflows into an iterative procedure that retrieves simultaneously surface reflectance and AOD, where the main improvement is a detailed characterization of the background land radiance, through a better characterization of SSI and surface BRDF. The better characterization of the land background radiance leads to a much better separation of the land and atmospheric signals captured by measurements of the TOA upwelling radiance by a space-borne imaging radiometer such as MODIS. In this study, we describe the retrieval of SSI only for the sake of readability, while other components and the complete workflow are described in other manuscripts in preparation.

E. Future Improvements of Our Method

The evaluation of SSI retrievals against ground measurements was limited by the fact that only total SSI was measured at Linzhi, MAWORS, and QOMS, and only in one case (Dali Station), both direct and diffuse irradiances were measured. Regarding the comparison of in situ measurements and satellite retrievals, further experiments to evaluate separately the effects of terrain on each SSI component would be highly relevant. In addition, this study describes a method to estimate instantaneous SSI at the time of MODIS overpass, which is based on the simultaneous characterization of cloud cover. The MOD06 cloud product includes retrievals of various cloud properties, such as cloud optical thickness, cf, and cloud top pressure, which are essential to parameterize the transmittance of a cloudy atmosphere, as applied in our method. We acknowledge that the retrieval of time-integrated, e.g., daily, SSI would require data at higher temporal resolution, i.e., as acquired by sensors onboard geostationary satellites. Besides, the 1 × 1 km MOD06 cloud product used in the study may not have sufficient spatial resolution to capture the fine-scale details of small or fragmented clouds, particularly over the Tibetan Plateau.

Regarding the in situ measurements, we plan to repeat and expand the experiment described by Roupioz et al. [78], which used hemispherical images to characterize not only the cf but also the angular distribution of clouds. These observations were applied by Roupioz et al. [78] to investigate the impact of the spatial organization of clouds on the four components of SSI. Addressing these issues will contribute to better understanding and improving the accuracy of SSI retrievals.

Regarding the terrain effect, our method considers the illumination angle, the impact of shadows, and the radiation reflected by the surrounding slopes. At present, estimates at a spatial resolution of 1 km can be obtained. The impact of the land cover heterogeneity within our 1 × 1 km pixels should be further investigated by combining the DEM with land cover data with a higher spatial resolution. Given the strong radiative interaction between the land surface and the atmosphere, retrievals of land surface properties should be fully coupled with retrievals of the atmospheric conditions.

A major heritage in our method and algorithms is the approach developed by Roupioz et al. [33], which uses subpixel topographic information to improve the accuracy of surface reflectance retrievals. Specifically, Roupioz et al. [33] used subpixel information on topography and land cover to estimate pixelwise terrain irradiance to improve the retrieval of pixelwise reflectance. Kustas [84] also emphasized the impact of subpixel heterogeneity on pixel average fluxes. In addition, Wen et al. [85] demonstrated the scale effect and correction of land-surface albedo in rugged terrain. Liu et al. [86] showed that subpixel information can improve the characterization of pixel land surface albedo. Subpixel variability in the BRDF should also be taken into account, as shown by Román et al. [87], who retrieved the BRDF at different spatial scales over a mixed agricultural landscape from airborne and satellite spectral measurements. All these studies demonstrate that the inclusion of subpixel topography and land cover is useful to improve the accuracy of surface irradiance and reflectance estimates in rugged terrains. Improvements can be achieved in future studies by considering the effects of the spatial variability of the terrain at the subpixel level using high spatial resolution DEM data and a downscaling method.

VI. Conclusion

In this study, we developed a method for quantifying the instantaneous SSI and its four components—the direct, isotropic diffuse, circumsolar diffuse, and terrain irradiances—on the Tibetan Plateau. The method applies MODIS, ERA5 reanalysis, and CALIOP data products, as well as DEM data. This method was developed by considering the coupled effects of the topography and atmosphere in the parameterization and LUT approaches, which are both based on physically based radiative transfer models.

The method developed in this study uses either MODIS data products or ERA5 data to characterize the atmospheric conditions for application in the parameterization and LUT schemes, respectively. The use of ozone and water vapor vertical profiles as close as possible to actual conditions is important for retrieving a more accurate SSI. This is achieved by using the ERA5 reanalysis data as input into MODTRAN. The comparability of the two schemes is also crucial to the accuracy of the derived SSI. Our results on this comparison support the use of the LUT method to fill gaps in the MODIS retrievals. The comparability of the two schemes was also verified using ground observations from four stations on the Tibetan Plateau. It was proven that the instantaneous SSI, estimated by combining the two schemes, is in satisfactory agreement with the ground measurements (see Fig. 4). The estimations of the diffuse irradiance were evaluated separately against the only available ground observations recorded at the Dali Station, and the results were better than our total SSI estimates, with R^2, RMSE, and relative BIAS values of 0.705, 94.98 W/m^2, and 31%, respectively.

We consider the main achievement of this study to be the provision of a feasible method for estimating the instantaneous SSI and its four components. The main advantage of this method is that it considers the coupled effects of the topography and atmosphere, and the combined use of the two schemes supports the continuity of the time series of the SSI and its four components at a 1-km spatial resolution.

Future work on the estimation of time-integrated SSI will require the use of other high temporal and spatial resolution atmospheric remote sensing products and DEM data to estimate the SSI and its four components. At present, for example, the data acquired by the second-generation FY-4 geostationary meteorological satellite [88], Pathfinder Atmospheres Extended (PATMOS-x) data, and Himawari-8 data [65] have a much higher temporal resolution and a fine spatial resolution, which makes it feasible to extend the use of our method to study land–atmosphere interactions on the

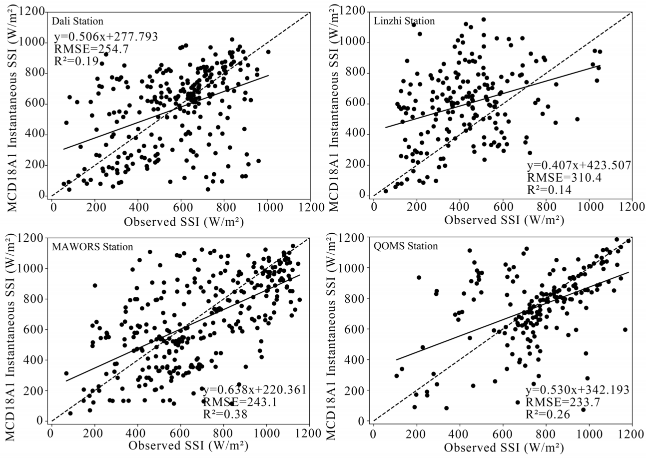

Fig. A-I. MCD18A1 instantaneous SSI against ground observations at Dali, Linzhi, MAWORS, and QOMS Stations in 2018 at the MODIS Aqua overpass time.

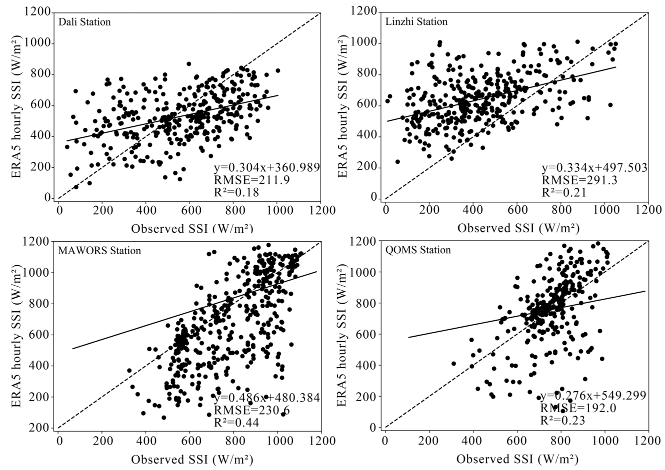

Fig. A-II. ERA5 hourly SSI against SSI observations at Dali, Linzhi, MAWORS, and QOMS Stations in 2018 at the MODIS Aqua overpass time.

Tibetan Plateau. Furthermore, the terrain parameters were used at a 1-km spatial resolution. In the future, we will use high spatial resolution DEM data to consider the effects of the spatial variability of the terrain at the subpixel level.

The satisfactory validation on the Tibetan Plateau suggests that this first attempt may lead to applications in rugged and complex terrains for long-term data products.

Appendix

A. Estimation of Extraterrestrial Solar Irradiance E_0

E_0 is expressed as

$$E_0 = S_0 \cdot \mathrm{SE}_d \tag{A-1}$$

where S_0 is the TOA solar constant (1367 W/m^2) and SE_d is the Sun–Earth distance in astronomical units (AU) with one AU being the mean Sun–Earth distance ($\approx 1.496 \times 10^8$ km)

$$\begin{aligned}\mathrm{SE}_d = 1/(&1.00011 + 0.034221\cos\mathrm{I} \\ &+ 0.00128\sin\mathrm{I} + 0.000719\cos2\mathrm{I} \\ &+ 0.000077\sin2\mathrm{I})^{1/2}\end{aligned} \tag{A-2}$$

where $\mathrm{I} = (2\pi d/365)$ and d is the day of the year. The amount of solar radiation reaching the Earth is inversely proportional to the square root of the Earth's distance from the Sun.

B. Construction of LUT

In this study, when MODIS atmosphere data products were not available, synthetic atmospheric profiles were generated using ERA5 reanalysis data and CALIOP 5-km aerosol profiles, and these data were input into MODTRAN to generate LUTs. The irradiance parameters E_d and E_h were estimated through the LUTs. The aerosol extinction of the CALIOP 5-km aerosol profile was converted into the meteorological visibility (VIS), which was defined using Koschmieder's [89] equation

$$\mathrm{VIS} = \frac{\ln(50)}{\mathrm{EXT550} + 0.1159}. \tag{A-3}$$

The MODTRAN parameter settings for the LUT are presented in Table V. The latitude and longitude values were defined according to the minimum and maximum limits of the study area, and then, a simulation was computed every 1°. The atmospheric profiles were synthesized according to the MODIS overpass time using ERA5 hourly pressure level data. The time was chosen to be 8:00 UTC during the daytime, which was approximately the overpass time of Aqua MODIS. Two surface reflectance values were defined to estimate the spherical albedo.

C. Scatter Plot Comparing With MCD18A1 and EAR5 SSI Products

See Figs. A-I and A-II.

D. Percentage of Missing Data for the Atmospheric MYD08 D3 Products for the Tibetan Plateau

See Table VI.

Acknowledgment

The authors thank the Institute of Tibetan Plateau Research of the Chinese Academy of Sciences and the Dali National Climate Observatory for providing valuable ground observation data. They also thank the Moderate Resolution Imaging Spectrometer (MODIS) Team for the freely distributed data downloaded from LAADS (Level-1 and Atmosphere Archive & Distribution System) (https://ladsweb.nascom.nasa.gov/search), the Cloud-Aerosol LiDAR and Infrared Pathfinder Satellite Observation (CALIPSO) Team for providing the Cloud-Aerosol LiDAR With Orthogonal Polarization (CALIOP) data (downloaded from the website: https://www-calipso.larc.nasa.gov/products/), and the ERA5 reanalysis data (downloaded from the website: https://www.ecmwf.int/en/forecasts/datasets).

References

[1] S. Sandmeier and K. I. Itten, "A physically-based model to correct atmospheric and illumination effects in optical satellite data of rugged terrain," *IEEE Trans. Geosci. Remote Sens.*, vol. 35, no. 3, pp. 708–717, May 1997, doi: 10.1109/36.581991.

[2] J. K. B. Bishop and W. B. Rossow, "Spatial and temporal variability of global surface solar irradiance," *J. Geophys. Res., Oceans*, vol. 96, no. C9, pp. 16839–16858, Sep. 1991, doi: 10.1029/91jc01754.

[3] C. Emde et al., "The libRadtran software package for radiative transfer calculations (version 2.0.1)," *Geosci. Model Develop.*, vol. 9, no. 5, pp. 1647–1672, May 2016, doi: 10.5194/gmd-9-1647-2016.

[4] Y. Chen, F. Weng, Y. Han, and Q. Liu, "Validation of the community radiative transfer model by using CloudSat data," *J. Geophys. Res., Atmos.*, vol. 113, no. D8, Jul. 2008, Art. no. D00A03, doi: 10.1029/2007jd009561.

[5] S. Fritz, P. K. Rao, and M. Weinstein, "Satellite measurements of reflected solar energy and the energy received at the ground," (in English), *J. Atmos. Sci.*, vol. 21, no. 2, pp. 141–151, 1964, doi: 10.1175/1520-0469(1964)021<0141:SMORSE>2.0.CO;2.

[6] J. D. Tarpley, "Estimating incident solar radiation at the surface from geostationary satellite data," *J. Appl. Meteorol.*, vol. 18, no. 9, pp. 1172–1181, Sep. 1979, doi: 10.1175/1520-0450(1979)018<1172:EISRAT>2.0.CO;2.

[7] S. Liang, D. Wang, T. He, and Y. Yu, "Remote sensing of Earth's energy budget: Synthesis and review," *Int. J. Digit. Earth*, vol. 12, no. 7, pp. 737–780, Mar. 2019, doi: 10.1080/17538947.2019.1597189.

[8] D. Cano et al., "A method for the determination of the global solar radiation from meteorological satellite data," *Sol. Energy*, vol. 37, no. 1, pp. 31–39, Jan. 1986, doi: 10.1016/0038-092x(86)90104-0.

[9] A. Hammer et al., "Solar energy assessment using remote sensing technologies," *Remote Sens. Environ.*, vol. 86, no. 3, pp. 423–432, Aug. 2003, doi: 10.1016/s0034-4257(03)00083-x.

[10] R. W. Mueller, C. Matsoukas, A. Gratzki, H. D. Behr, and R. Hollmann, "The CM-SAF operational scheme for the satellite based retrieval of solar surface irradiance—A LUT based eigenvector hybrid approach," *Remote Sens. Environ.*, vol. 113, no. 5, pp. 1012–1024, May 2009, doi: 10.1016/j.rse.2009.01.012.

[11] R. Posselt, R. W. Mueller, R. Stöckli, and J. Trentmann, "Remote sensing of solar surface radiation for climate monitoring—The CM-SAF retrieval in international comparison," *Remote Sens. Environ.*, vol. 118, pp. 186–198, Mar. 2012, doi: 10.1016/j.rse.2011.11.016.

[12] L. Wang, W. Gong, B. Hu, A. Lin, H. Li, and L. Zou, "Modeling and analysis of the spatiotemporal variations of photosynthetically active radiation in China during 1961–2012," *Renew. Sustain. Energy Rev.*, vol. 49, pp. 1019–1032, Sep. 2015, doi: 10.1016/j.rser.2015.04.174.

[13] B. Leckner, "The spectral distribution of solar radiation at the Earth's surface—Elements of a model," *Sol. Energy*, vol. 20, no. 2, pp. 143–150, 1978, doi: 10.1016/0038-092x(78)90187-1.

[14] C. A. Gueymard, "Turbidity determination from broadband irradiance measurements: A detailed multicoefficient approach," *J. Appl. Meteorol.*, vol. 37, no. 4, pp. 414–435, 1998, doi: 10.1175/1520-0450(1998)037<0414:TDFBIM>2.0.CO;2.

[15] K. Yang, T. Koike, G. Huang, and N. Tamai, "Development and validation of an advanced model for estimating solar radiation from surface meteorological data," in *Recent Developments in Solar Energy*, T. P. Hough, Ed. Hauppauge, NY, USA: Nova Science, 2007, ch. 1, pp. 1–54.

[16] M. Iqbal, *An Introduction to Solar Radiation*. Cambridge, MA, USA: Academic Press, 1983.

[17] K. Yang, G. W. Huang, and N. Tamai, "A hybrid model for estimating global solar radiation," *Sol. Energy*, vol. 70, no. 1, pp. 13–22, 2001, doi: 10.1016/s0038-092x(00)00121-3.

[18] S. Liang et al., "Mapping high-resolution incident photosynthetically active radiation over land from polar-orbiting and geostationary satellite data," *Photogramm. Eng. Remote Sens.*, vol. 73, no. 10, pp. 1085–1089, Oct. 2007.

[19] H. Zhang, C. Huang, S. Yu, L. Li, X. Xin, and Q. Liu, "A lookup-table-based approach to estimating surface solar irradiance from geostationary and polar-orbiting satellite data," *Remote Sens.*, vol. 10, no. 3, p. 411, Mar. 2018, doi: 10.3390/rs10030411.

[20] Y. Zhang, T. He, S. Liang, D. Wang, and Y. Yu, "Estimation of all-sky instantaneous surface incident shortwave radiation from moderate resolution imaging spectroradiometer data using optimization method," *Remote Sens. Environ.*, vol. 209, pp. 468–479, May 2018, doi: 10.1016/j.rse.2018.02.052.

[21] T. Wang, G. Yan, and L. Chen, "Consistent retrieval methods to estimate land surface shortwave and longwave radiative flux components under clear-sky conditions," *Remote Sens. Environ.*, vol. 124, pp. 61–71, Sep. 2012, doi: 10.1016/j.rse.2012.04.026.

[22] Y. Ryu, C. Jiang, H. Kobayashi, and M. Detto, "MODIS-derived global land products of shortwave radiation and diffuse and total photosynthetically active radiation at 5 km resolution from 2000," *Remote Sens. Environ.*, vol. 204, pp. 812–825, Jan. 2018, doi: 10.1016/j.rse.2017.09.021.

[23] L. Yang, X. Zhang, S. Liang, Y. Yao, K. Jia, and A. Jia, "Estimating surface downward shortwave radiation over China based on the gradient boosting decision tree method," *Remote Sens.*, vol. 10, no. 2, p. 185, Jan. 2018, doi: 10.3390/rs10020185.

[24] G. Yan et al., "Temporal extrapolation of daily downward shortwave radiation over cloud-free rugged terrains. Part 1: Analysis of topographic effects," *IEEE Trans. Geosci. Remote Sens.*, vol. 56, no. 11, pp. 6375–6394, Nov. 2018, doi: 10.1109/TGRS.2018.2838143.

[25] D. Hao et al., "Impacts of DEM geolocation bias on downward surface shortwave radiation estimation over clear-sky rugged terrain: A case study in Dayekou Basin, China," *IEEE Geosci. Remote Sens. Lett.*, vol. 16, no. 1, pp. 10–14, Jan. 2019, doi: 10.1109/LGRS.2018.2868563.

[26] T. Wang, G. Yan, X. Mu, Z. Jiao, L. Chen, and Q. Chu, "Toward operational shortwave radiation modeling and retrieval over rugged terrain," *Remote Sens. Environ.*, vol. 205, pp. 419–433, Feb. 2018, doi: 10.1016/j.rse.2017.11.006.

[27] R. Stöckli and R. Stöckli, "The HelioMont surface solar radiation processing," in *Bundesamt Für Meteorologie Und Klimatologie*. Zurich, Switzerland: MeteoSchweiz, Federal Department of Home Affairs FDHA, 2013.

[28] L. M. Mercado et al., "Impact of changes in diffuse radiation on the global land carbon sink," *Nature*, vol. 458, no. 7241, pp. 1014–1017, Apr. 2009, doi: 10.1038/nature07949.

[29] V. Ramanathan and G. Carmichael, "Global and regional climate changes due to black carbon," *Nat. Geosci.*, vol. 1, no. 4, pp. 221–227, 2008, doi: 10.1038/ngeo156.

[30] M. Wild, A. Ohmura, and K. Makowski, "Impact of global dimming and brightening on global warming," *Geophys. Res. Lett.*, vol. 34, no. 4, Feb. 2007, doi: 10.1029/2006gl028031.

[31] C. Xing et al., "Ground-based vertical profile observations of atmospheric composition on the Tibetan Plateau (2017–2019)," *Earth Syst. Sci. Data*, vol. 13, no. 10, pp. 4897–4912, Oct. 2021, doi: 10.5194/essd-13-4897-2021.

[32] G. Huang et al., "Estimating surface solar irradiance from satellites: Past, present, and future perspectives," *Remote Sens. Environ.*, vol. 233, Nov. 2019, Art. no. 111371, doi: 10.1016/j.rse.2019.111371.

[33] L. Roupioz, F. Nerry, L. Jia, and M. Menenti, "Improved surface reflectance from remote sensing data with sub-pixel topographic information," *Remote Sens.*, vol. 6, no. 11, pp. 10356–10374, Oct. 2014, doi: 10.3390/rs61110356.

[34] W. Tang, K. Yang, Z. Sun, J. Qin, and X. Niu, "Global performance of a fast parameterization scheme for estimating surface solar radiation from MODIS data," *IEEE Trans. Geosci. Remote Sens.*, vol. 55, no. 6, pp. 3558–3571, Jun. 2017, doi: 10.1109/TGRS.2017.2676164.

[35] C. Xu, Y. M. Ma, C. You, and Z. K. Zhu, "The regional distribution characteristics of aerosol optical depth over the Tibetan Plateau," *Atmos. Chem. Phys.*, vol. 15, no. 20, pp. 12065–12078, Oct. 2015, doi: 10.5194/acp-15-12065-2015.

[36] M. Pokharel et al., "Aerosol properties over Tibetan Plateau from a decade of AERONET measurements: Baseline, types, and influencing factors," *J. Geophys. Res., Atmos.*, vol. 124, no. 23, pp. 13357–13374, Dec. 2019, doi: 10.1029/2019jd031293.

[37] Y. Liu, Y. Sato, R. Jia, Y. Xie, J. Huang, and T. Nakajima, "Modeling study on the transport of summer dust and anthropogenic aerosols over the Tibetan Plateau," *Atmos. Chem. Phys.*, vol. 15, no. 21, pp. 12581–12594, Nov. 2015, doi: 10.5194/acp-15-12581-2015.

[38] C. Zhao et al., "Aerosol characteristics and impacts on weather and climate over the Tibetan Plateau," *Nat. Sci. Rev.*, vol. 7, no. 3, pp. 492–495, Mar. 2020, doi: 10.1093/nsr/nwz184.

[39] S. Kang et al., "Linking atmospheric pollution to cryospheric change in the third pole region: Current progress and future prospects," *Nat. Sci. Rev.*, vol. 6, no. 4, pp. 796–809, Jul. 2019.

[40] R. Jia, Y. Liu, S. Hua, Q. Zhu, and T. Shao, "Estimation of the aerosol radiative effect over the Tibetan Plateau based on the latest CALIPSO product," *J. Meteorol. Res.*, vol. 32, no. 5, pp. 707–722, Oct. 2018, doi: 10.1007/s13351-018-8060-3.

[41] T. Gerken et al., "Turbulent flux modelling with a simple 2-layer soil model and extrapolated surface temperature applied at Nam Co Lake basin on the Tibetan Plateau," *Hydrol. Earth Syst. Sci.*, vol. 16, no. 4, pp. 1095–1110, Apr. 2012, doi: 10.5194/hess-16-1095-2012.

[42] Y. Ma et al., "A long-term (2005–2016) dataset of hourly integrated land–atmosphere interaction observations on the Tibetan Plateau," *Earth Syst. Sci. Data*, vol. 12, no. 4, pp. 2937–2957, Nov. 2020, doi: 10.5194/essd-12-2937-2020.

[43] H. Liu, J. Feng, J. Sun, L. Wang, and A. Xu, "Eddy covariance measurements of water vapor and CO_2 fluxes above the Erhai Lake," *Sci. China Earth Sci.*, vol. 58, no. 3, pp. 317–328, Mar. 2015, doi: 10.1007/s11430-014-4828-1.

[44] C.-S. Zhu et al., "Black carbon aerosols at Mt. Muztagh Ata, a high-altitude location in the Western Tibetan Plateau," *Aerosol Air Quality Res.*, vol. 16, no. 3, pp. 752–763, 2016, doi: 10.4209/aaqr.2015.04.0255.

[45] R. Wang and Y. Ma, "Comparative analyses on radiation characteristics in different areas over the Tibetan Plateau," in *Plateau Meteorology*, vol. 29, no. 2. Lanzhou, China, 2010, pp. 251–259.

[46] D. M. Winker, M. A. Vaughan, A. Omar, Y. Hu, and K. A. Powell, "Overview of the CALIPSO mission and CALIOP data processing algorithms," *J. Atmos. Ocean. Technol.*, vol. 26, no. 11, pp. 2310–2323, 2009, doi: 10.1175/2009jtecha1281.1.

[47] D. M. Winker, Z. Liu, A. Omar, J. Tackett, and D. Fairlie, "CALIOP observations of the transport of ash from the Eyjafjallajökull volcano in April 2010," *J. Geophys. Res., Atmos.*, vol. 117, no. D20, Mar. 2012, Art. no. D00U15, doi: 10.1029/2011jd016499.

[48] D. M. Winker, J. L. Tackett, B. J. Getzewich, Z. Liu, M. A. Vaughan, and R. R. Rogers, "The global 3-D distribution of tropospheric aerosols as characterized by CALIOP," *Atmos. Chem. Phys.*, vol. 13, no. 6, pp. 3345–3361, Mar. 2013, doi: 10.5194/acp-13-3345-2013.

[49] P. Li et al., "Evaluation of ASTER GDEM using GPS benchmarks and SRTM in China," *Int. J. Remote Sens.*, vol. 34, no. 5, pp. 1744–1771, Mar. 2013, doi: 10.1080/01431161.2012.726752.

[50] J. E. Hay, "Calculation of monthly mean solar radiation for horizontal and inclined surfaces," *Sol. Energy*, vol. 23, no. 4, pp. 301–307, 1979, doi: 10.1016/0038-092x(79)90123-3.

[51] J. Dozier, "Spectral signature of Alpine snow cover from the Landsat thematic mapper," *Remote Sens. Environ.*, vol. 28, pp. 9–22, Apr./Jun. 1989, doi: 10.1016/0034-4257(89)90101-6.

[52] C. R. Duguay, "An approach to the estimation of surface net radiation in mountain areas using remote sensing and digital terrain data," *Theor. Appl. Climatol.*, vol. 52, nos. 1–2, pp. 55–68, 1995, doi: 10.1007/bf00865507.

[53] S. Gupta, D. Kratz, P. W. Stackhouse Jr., and A. Wilber, "The Langley parameterized shortwave algorithm (LPSA) for surface radiation budget studies," NASA Langley Res. Center, Hampton, VA, USA, Tech. Rep. NASA/TP-2001-211272, Dec. 2001.

[54] K. Zakšek, K. Oštir, and Ž. Kokalj, "Sky-view factor as a relief visualization technique," *Remote Sens.*, vol. 3, no. 2, pp. 398–415, 2011, doi: 10.3390/rs3020398.

[55] G. L. Stephens, "Radiation profiles in extended water clouds. II: Parameterization schemes," *J. Atmos. Sci.*, vol. 35, no. 11, pp. 2123–2132, 1978, doi: 10.1175/1520-0469(1978)035<2123:RPIEWC>2.0.CO;2.

[56] G. L. Stephens, S. Ackerman, and E. A. Smith, "A shortwave parameterization revised to improve cloud absorption," *J. Atmos. Sci.*, vol. 41, no. 4, pp. 687–690, 1984, doi: 10.1175/1520-0469(1984)041<0687:ASPRTI>2.0.CO;2.

[57] P. E. Van Laake and G. A. Sanchez-Azofeifa, "Simplified atmospheric radiative transfer modelling for estimating incident PAR using MODIS atmosphere products," *Remote Sens. Environ.*, vol. 91, no. 1, pp. 98–113, May 2004, doi: 10.1016/j.rse.2004.03.002.

[58] L. Roupioz, L. Jia, F. Nerry, and M. Menenti, "Estimation of daily solar radiation budget at kilometer resolution over the Tibetan Plateau by integrating MODIS data products and a DEM," *Remote Sens.*, vol. 8, no. 6, p. 504, Jun. 2016, doi: 10.3390/rs8060504.

[59] W. Du et al., "Chemical characterization of submicron aerosol and particle growth events at a national background site (3295 m a.s.l.) on the Tibetan Plateau," *Atmos. Chem. Phys.*, vol. 15, no. 18, pp. 10811–10824, Sep. 2015, doi: 10.5194/acp-15-10811-2015.

[60] J. Xu et al., "Dissolved organic matter and inorganic ions in a central Himalayan glacier—Insights into chemical composition and atmospheric sources," *Environ. Sci. Technol.*, vol. 47, no. 12, pp. 6181–6188, May 2013, doi: 10.1021/es4009882.

[61] C. You, C. Xu, B. Xu, H. Zhao, and L. Song, "Levoglucosan evidence for biomass burning records over Tibetan glaciers," *Environ. Pollut.*, vol. 216, pp. 173–181, Sep. 2016, doi: 10.1016/j.envpol.2016.05.074.

[62] H.-Y. Kim and S. Liang, "Development of a hybrid method for estimating land surface shortwave net radiation from MODIS data," *Remote Sens. Environ.*, vol. 114, no. 11, pp. 2393–2402, Nov. 2010, doi: 10.1016/j.rse.2010.05.012.

[63] S. Gui, S. Liang, and L. Li, "Validation of surface radiation data provided by the CERES over the Tibetan Plateau," in *Proc. 17th Int. Conf. Geoinf.*, Fairfax, VA, USA, Aug. 2009, pp. 1–6, doi: 10.1109/GEOINFORMATICS.2009.5292880.

[64] G. Huang, M. Ma, S. Liang, S. Liu, and X. Li, "A LUT-based approach to estimate surface solar irradiance by combining MODIS and MTSAT data," *J. Geophys. Res., Atmos.*, vol. 116, no. D22, Nov. 2011, Art. no. D22201, doi: 10.1029/2011jd016120.

[65] Y.-C. Yu, J. Shi, T. Wang, H. Letu, and C. Zhao, "All-sky total and direct surface shortwave downward radiation (SWDR) estimation from satellite: Applications to MODIS and Himawari-8," *Int. J. Appl. Earth Observ. Geoinf.*, vol. 102, Oct. 2021, Art. no. 102380, doi: 10.1016/j.jag.2021.102380.

[66] X. J. Zhou, C. Luo, W. L. Li, and J. E. Shi, "Variation of total ozone in China and low value center of Tibetan Plateau," (in Chinese), *Chin. Sci. Bull.*, vol. 40, no. 15, pp. 1396–1398, Aug. 1995, doi: 10.3321/j.issn:0023-074X.1995.15.016.

[67] S. Vanonckelen, S. Lhermitte, V. Balthazar, and A. Van Rompaey, "Performance of atmospheric and topographic correction methods on Landsat imagery in mountain areas," *Int. J. Remote Sens.*, vol. 35, no. 13, pp. 4952–4972, Jul. 2014, doi: 10.1080/01431161.2014.933280.

[68] Y. Zhang and Z. Li, "Remote sensing of atmospheric fine particulate matter ($PM_{2.5}$) mass concentration near the ground from satellite observation," *Remote Sens. Environ.*, vol. 160, pp. 252–262, Apr. 2015, doi: 10.1016/j.rse.2015.02.005.

[69] E. Ezhova et al., "Direct effect of aerosols on solar radiation and gross primary production in boreal and Hemiboreal forests," *Atmos. Chem. Phys.*, vol. 18, no. 24, pp. 17863–17881, Dec. 2018, doi: 10.5194/acp-18-17863-2018.

[70] B. Hu et al., "Quantification of the impact of aerosol on broadband solar radiation in North China," *Sci. Rep.*, vol. 7, no. 1, p. 44851, Mar. 2017, doi: 10.1038/srep44851.

[71] X. Li, F. Wagner, W. Peng, J. Yang, and D. L. Mauzerall, "Reduction of solar photovoltaic resources due to air pollution in China," *Proc. Nat. Acad. Sci. USA*, vol. 114, no. 45, pp. 11867–11872, Nov. 2017, doi: 10.1073/pnas.1711462114.

[72] J. Li, Y. Jiang, X. Xia, and Y. Hu, "Increase of surface solar irradiance across East China related to changes in aerosol properties during the past decade," *Environ. Res. Lett.*, vol. 13, no. 3, Mar. 2018, Art. no. 034006, doi: 10.1088/1748-9326/aaa35a.

[73] X. Pedruzo-Bagazgoitia, H. G. Ouwersloot, M. Sikma, C. C. van Heerwaarden, C. M. J. Jacobs, and J. V.-G. de Arellano, "Direct and diffuse radiation in the shallow cumulus–vegetation system: Enhanced and decreased evapotranspiration regimes," *J. Hydrometeorol.*, vol. 18, no. 6, pp. 1731–1748, Jun. 2017, doi: 10.1175/jhm-d-16-0279.1.

[74] S. J. Cheng, A. L. Steiner, D. Y. Hollinger, G. Bohrer, and K. J. Nadelhoffer, "Using satellite-derived optical thickness to assess the influence of clouds on terrestrial carbon uptake," *J. Geophys. Res., Biogeosci.*, vol. 121, no. 7, pp. 1747–1761, Jul. 2016, doi: 10.1002/2016jg003365.

[75] Q. Min, "Impacts of aerosols and clouds on forest-atmosphere carbon exchange," *J. Geophys. Res., Atmos.*, vol. 110, no. D6, Mar. 2005, Art. no. D06203, doi: 10.1029/2004jd004858.

[76] J. Qiu, "Broadband extinction method to determine aerosol optical depth from accumulated direct solar radiation," (in English), *J. Appl. Meteorol.*, vol. 42, no. 11, pp. 1611–1625, 2003, doi: 10.1175/1520-0450(2003)042<1611:BEMTDA>2.0.CO;2.

[77] I. Vardavas and F. Taylor, *Radiation and Climate* (International Series of Monographs on Physics), vol. 138. London, U.K.: Oxford Univ. Press, 2007.

[78] L. Roupioz, J. Colin, L. Jia, F. Nerry, and M. Menenti, "Quantifying the impact of cloud cover on ground radiation flux measurements using hemispherical images," *Int. J. Remote Sens.*, vol. 36, nos. 19–20, pp. 5087–5104, Oct. 2015, doi: 10.1080/01431161.2015.1084440.

[79] A. Damiani et al., "An intensive campaign-based intercomparison of cloud optical depth from ground and satellite instruments under overcast conditions," *SOLA*, vol. 15, pp. 198–204, Aug. 2019, doi: 10.2151/sola.2019-036.

[80] Y. Wu, M. de Graaf, and M. Menenti, "Improved MODIS dark target aerosol optical depth algorithm over land: Angular effect correction," *Atmos. Meas. Techn.*, vol. 9, no. 11, pp. 5575–5589, Nov. 2016, doi: 10.5194/amt-9-5575-2016.

[81] Y. Wu, M. de Graaf, M. Menenti, and G. de Leeuw, "MODIS aerosol optical depth retrieval over land considering surface BRDF effects," in *Proc. Geophys. Res. Meeting Abstr.*, vol. 18, 2016, Paper nos. 1607-7962.

[82] Y. Wu, M. de Graaf, and M. Menenti, "The sensitivity of AOD retrieval to aerosol type and vertical distribution over land with MODIS data," *Remote Sens.*, vol. 8, no. 9, p. 765, Sep. 2016, doi: 10.3390/rs8090765.

[83] Y. Wu, M. de Graaf, and M. Menenti, "The impact of aerosol vertical distribution on aerosol optical depth retrieval using CALIPSO and MODIS data: Case study over dust and smoke regions," *J. Geophys. Res., Atmos.*, vol. 122, no. 16, pp. 8801–8815, Aug. 2017, doi: 10.1002/2016jd026355.

[84] W. Kustas, "Evaluating the effects of subpixel heterogeneity on pixel average fluxes," *Remote Sens. Environ.*, vol. 74, no. 3, pp. 327–342, Dec. 2000, doi: 10.1016/s0034-4257(99)00081-4.

[85] J. Wen, Q. Liu, Q. Liu, Q. Xiao, and X. Li, "Scale effect and scale correction of land-surface albedo in rugged terrain," *Int. J. Remote Sens.*, vol. 30, no. 20, pp. 5397–5420, Sep. 2009, doi: 10.1080/01431160903130903.

[86] W. Liu, B. Hu, and S. Wang, "Improving land surface pixel level albedo characterization using sub-pixel information retrieved from remote sensing," in *Proc. EEE Int. Geosci. Remote Sens. Symp.*, Jul. 2008, pp. 7–11, doi: 10.1109/IGARSS.2008.4779115.

[87] M. O. Román, C. K. Gatebe, C. B. Schaaf, R. Poudyal, Z. Wang, and M. D. King, "Variability in surface BRDF at different spatial scales (30 m–500 m) over a mixed agricultural landscape as retrieved from airborne and satellite spectral measurements," *Remote Sens. Environ.*, vol. 115, no. 9, pp. 2184–2203, Sep. 2011, doi: 10.1016/j.rse.2011.04.012.

[88] J. Yang, Z. Zhang, C. Wei, F. Lu, and Q. Guo, "Introducing the new generation of Chinese geostationary weather satellites, Fengyun-4," *Bull. Amer. Meteorol. Soc.*, vol. 98, no. 8, pp. 1637–1658, Aug. 2017, doi: 10.1175/bams-d-16-0065.1.

[89] H. Koschmieder, "Theorie der horizontalen Sechtweite," (in German), *Beitr. Phys. Atmos.*, vol. 12, pp. 33–53, Jan. 1924.

Junru Jia received the M.S. degree from Shandong Agricultural University, Taian, China, in 2018. She is currently pursuing the Ph.D. degree in cartography and geographic information systems with the Aerospace Information Research Institute, Chinese Academy of Sciences, Beijing, China.

Her research interests include modeling the interaction of radiation with atmosphere–land in rugged terrain and retrieval of atmospheric aerosol optical depth (AOD) and land surface bidirectional reflectance distribution function (BRDF)/albedo.

Massimo Menenti is an internationally renowned scientist in the fields of Earth observation and the global terrestrial water cycle. He held senior research positions in The Netherlands, France, the United States, China, and Italy. He has coordinated many large European projects with participants from Europe, Asia, the United States, and Africa. His best known achievements have been attained in the aspects of surface parameter retrievals from remote sensing, remote sensing-based evapotranspiration (ET) estimation, time-series analysis of remote sensing products, and the application of remote sensing technology in hydrology and climate models. He initiated the use of remote sensing (RS) to assess and monitor crop water requirements and irrigation performance in the late 1980s confirmed by the numerous publications in the field. He is one of the earliest researchers to use laser radar technology to measure surface aerodynamic roughness. He initiated the use of time-series analysis techniques to extract information from satellite data. He presented the surface energy balance index (SEBI) theory for ET estimation, which is the prototype of the simplified-surface energy balance index (S-SEBI), surface energy balance system (SEBS), and surface energy balance algorithm for land (SEBAL) models. He has published about 700 research articles. His works have been cited more than 15 000 times (https://scholar.google.com/citationsuser = iHUEl54AAAAJ&hl = nl).

Li Jia (Member, IEEE) received the Ph.D. degree in environmental science from Wageningen University & Research, Wageningen, The Netherlands, in 2004.

She is a leading scientist in Earth observation for terrestrial water cycle, water resources, and climate change at the Aerospace Information Research Institute, Chinese Academy of Sciences, Beijing, China. Her research interests include the study of Earth observation and its applications in hydrometeorology, water resources, agriculture, and climate change.

Dr. Jia is currently a member of the Global Energy and Water Exchanges Program-Scientific Steering Group (GEWEX-SSG).

Qiting Chen received the Ph.D. degree in cartography and geographic information systems from the Aerospace Information Research Institute, Chinese Academy of Sciences, Beijing, China, in 2017.

She is currently an Assistant Researcher with the Aerospace Information Research Institute, Chinese Academy of Sciences. Her research interests include atmosphere–land surface interaction.

Anlun Xu received the B.S. degree from Yunnan Normal University, Kunming, China, in 2005, and the M.S. degree from the Hefei Institutes of Physical Science, Chinese Academy of Sciences, Hefei, China, in 2008.

He is currently a Professor-level Senior Engineer with the Dali National Climate Observatory, Dali, China. His research interests include mountain meteorology, atmospheric boundary layer, and land–atmosphere interaction.